Transition to chaos of natural convection between two infinite differentially heated vertical plates

Zhenlan Gao*
CNRS, LIMSI, UPR3251, BP 133, 91403 Orsay Cedex, France and
Universite Pierre et Marie Curie-Paris 6, 4, Place Jussieu, 75252 Paris, Cedex 05, France

Anne Sergent
CNRS, LIMSI, UPR3251, BP 133, 91403 Orsay Cedex, France and
Universite Pierre et Marie Curie-Paris 6, 4, Place Jussieu, 75252 Paris, Cedex 05, France

Berengere Podvin†
CNRS, LIMSI, UPR3251, BP 133, 91403 Orsay Cedex, France

Shihe Xin
CETHIL, INSA de Lyon, 69621 Villeurbanne Cedex, France

Patrick Le Quéré
CNRS, LIMSI, UPR3251, BP 133, 91403 Orsay Cedex, France

Laurette S. Tuckerman
PMMH, ESPCI, 75005 Paris, France
(Received 15 April 2013; published 12 August 2013)

Natural convection of air between two infinite vertical differentially heated plates is studied analytically in two dimensions (2D) and numerically in two and three dimensions (3D) for Rayleigh numbers Ra up to 3 times the critical value $Ra_c = 5708$. The first instability is a supercritical circle pitchfork bifurcation leading to steady 2D corotating rolls. A Ginzburg-Landau equation is derived analytically for the flow around this first bifurcation and compared with results from direct numerical simulation (DNS). In two dimensions, DNS shows that the rolls become unstable via a Hopf bifurcation. As Ra is further increased, the flow becomes quasiperiodic, and then temporally chaotic for a limited range of Rayleigh numbers, beyond which the flow returns to a steady state through a spatial modulation instability. In three dimensions, the rolls instead undergo another pitchfork bifurcation to 3D structures, which consist of transverse rolls connected by counter-rotating vorticity braids. The flow then becomes time dependent through a Hopf bifurcation, as exchanges of energy occur between the rolls and the braids. Chaotic behavior subsequently occurs through two competing mechanisms: a sequence of period-doubling bifurcations leading to intermittency or a spatial pattern modulation reminiscent of the Eckhaus instability.

DOI: 10.1103/PhysRevE.88.023010 PACS number(s): 47.55.P−, 47.20.Ky, 47.20.Bp, 47.27.Cn

I. INTRODUCTION

Transition to turbulence of natural convection in a fluid layer between two differentially heated plates is of substantial interest for many industrial applications, such as heat exchangers in reactors or insulation of buildings (e.g., double-paned windows). In classic Rayleigh-Bénard convection, the fluid lies between two horizontal plates and is heated from below so the thermal gradient opposes the direction of gravity. In the configuration considered here, the walls are vertical, and the thermal gradient is orthogonal to the direction of gravity. Although this configuration may not have received quite as much attention as Rayleigh-Bénard convection [1], a number of studies have shed some light on its specific dynamics. However, with a few exceptions, most of the theory and numerics so far have focused either on the two-dimensional case or on a limited range around the critical Rayleigh number.

The first investigations of natural convection between differentially heated vertical plates relied on experimental descriptions. Elder [2] observed the onset of secondary flow and "cat's-eyes" tertiary flow in his experiments with two fluids: paraffin and silicone oil. Vest and Arpaci [3] observed the onset of secondary convection in air flow and compared it with their calculations of secondary flow stream patterns. Oshima [4] considered convection in a rectangular water-filled cavity heated through two vertical sidewalls. He observed the development of the wavy motions of streamlines into rows of periodic vortices, which then burst into turbulence.

Early computations of the flow structure were based on stability analysis in the neighborhood of the critical Rayleigh number Ra_c and were limited to the 2D case. Following Batchelor's [5] approach, Gill and Davey [6] and then Bergholz [7] investigated the 2D linear stability of the flow for different Prandtl numbers. Vest and Arpaci [3] also relied on 2D linear stability to calculate secondary-flow stream patterns. Weakly nonlinear stability calculations in 2D were carried out by Daniels and Weinstein [8], Cornet and Lamarque [9] for air, and Mizushima and Gotoh [10] for water convection. A

*gao@limsi.fr
†podvin@limsi.fr

Newton-Raphson method to compute equilibria was used by Mizushima and Saito [11] in the zero-Prandtl-number limit. More bifurcation diagrams were obtained in the case of air by Mizushima and Tanaka [12,13].

The agreement between the patterns predicted by theory and experimental observations of the first instabilities suggests that convection between 2D infinite plates is a good representation of what happens in tall cavities. However, there is some evidence that these simplified assumptions may not provide an accurate picture of the real dynamics. First, the influence of the aspect ratio—what exactly makes a cavity "tall enough"—may be difficult to determine intuitively. From Bergholz [7], it can be seen that the nature of the most unstable disturbances for water (Pr = 7.5) switches from a stationary to a traveling state for a critical aspect ratio $A \sim 70$. Moreover, the nature of the higher-order bifurcations is likely to be affected by the presence of horizontal boundaries. S. Xin [14] carried out 2D numerical simulations of natural convection of air in a confined cavity as well as between infinite plates (a channel). Transition to the chaotic state was observed at a relatively low Rayleigh number in the cavity, while only regular patterns could be obtained in the channel.

Second, although most numerical simulations [15–20] have been carried out in the 2D case, there is evidence that the flow becomes rapidly three-dimensional as the Rayleigh (or Grashof) number increases, as was observed by Wright *et al.* [21] in their experiments for tall air-filled cavities. This is in agreement with Chait and Korpela's [22] 3D linear stability calculations, which indicated that the flow between vertical isothermal sidewalls should become rapidly three-dimensional. Early 3D computations of equilibria in the limit of vanishing Prandtl number were performed by Nagata and Busse [23]. A steady 3D pattern was found to be associated with a secondary instability. Clever and Busse [24] also identified a steady 3D pattern, which then bifurcated into a traveling wave of invariant shape at higher Rayleigh numbers. A Ginzburg-Landau model was used by Suslov and Paolucci [25,26] to describe the three-dimensional flow between infinite plates in the case of non-Boussinesq convection for a variety of Prandtl numbers. However, their approach remains limited to a region around the critical Rayleigh number. Bratsun *et al.* [27] carried out extensive experimental and numerical studies of the successive bifurcations of the flow in three dimensions, but their work was conducted at a high Prandtl number (Pr = 26) for which the primary instability consists of traveling waves. No equivalent study has been performed for air as far as we know.

At the other end of the Rayleigh number range, the turbulent regime has received some attention for two decades. Phillips [28] compared 3D direct numerical simulation results with the experiments of Elder [29] and showed that most of the turbulence was generated by the shear layer at the center of the slot. Versteegh and Niewstadt [30,31] computed energy budgets to determine scaling laws and wall functions with a direct application to turbulence modeling. Although the presence of spiral structures has been noted by Wang *et al.* [32] for air at $\mathrm{Ra} = 5.4 \times 10^5$, a complete coherent-structure-based description is still missing. As noted by Hall [33], "there has been apparently no attempt to look for coherent structures embedded in the flows as has become routine in shear flows." Few models for the dynamics of such structures have yet been proposed [33].

The goal of the present study is to provide a description of the transition to turbulence of natural convection of air between two infinite plates. We are aware of the limited character of this investigation, which crucially depends on the periodic dimensions of the plates. Due to numerical constraints, the transverse dimension of the plates was kept small, which hampers the development of three-dimensional instabilities. However, we believe that such simulations constitute a necessary step towards a better understanding of the dynamics of unsteady natural convection. They also represent a complementary approach to linear stability analysis, where the full range of wave numbers can be explored. A detailed analysis of the flow at lower Rayleigh numbers could be helpful to understand the coherent structures observed in the fully developed turbulent regime [32]. Some direct numerical simulation (DNS) studies [30] suggest that a substantial part of the energy in the turbulent regime is associated with patterns which are similar to the most linearly unstable mode. This situation presents some analogy with Rayleigh-Bénard convection, where the large-scale structures identified in the turbulent regime share common features with the convection cells observed at near-critical Rayleigh numbers [1,34,35]. In addition, determining key instability mechanisms in a canonical configuration will be useful for studying more complex geometries and/or including additional physics such as radiation or mixed convection.

The paper is organized as follows. We first recall standard theoretical results based on linear and weakly nonlinear stability analysis. We derive analytically a Ginzburg-Landau equation to represent the flow around the first bifurcation. We then briefly present results for 2D direct numerical simulation for Rayleigh numbers Ra up to about $3\mathrm{Ra}_c$. We show that a temporally chaotic regime can only be found over a limited range of Rayleigh numbers. We then present our results of a 3D numerical simulation. The sequence of the instabilities leading to chaos and corresponding physics is described in detail. A large difference with 2D results is found.

II. PHYSICAL AND NUMERICAL CONFIGURATION

We consider the flow of air between two infinite vertical plates maintained at different temperatures. The configuration is represented in Fig. 1(a). The distance between the two plates is D, and the periodic height and depth of the plates are L_z and L_y, respectively. The temperature difference between the plates is set to ΔT. The x direction is normal to the plates, y represents the transverse direction, and the gravity g is opposite to the vertical direction z.

The relevant fluid properties are the kinetic viscosity ν, thermal diffusivity κ, and thermal expansion coefficient β. Four nondimensional parameters characterize the flow: the Prandtl number $\mathrm{Pr} = \nu/\kappa$, the respectively transverse and vertical aspect ratios $A_y = L_y/D$ and $A_z = L_z/D$, and the Rayleigh number based on the gap between the two plates $\mathrm{Ra} = \frac{g\beta\Delta T D^3}{\nu\kappa}$. Only the Rayleigh number dependence is considered in the present study. The Prandtl number is fixed and equal to 0.71. The transverse aspect ratio is set to be $A_y = 1$. The vertical aspect ratio was $A_z = 10$ in most cases

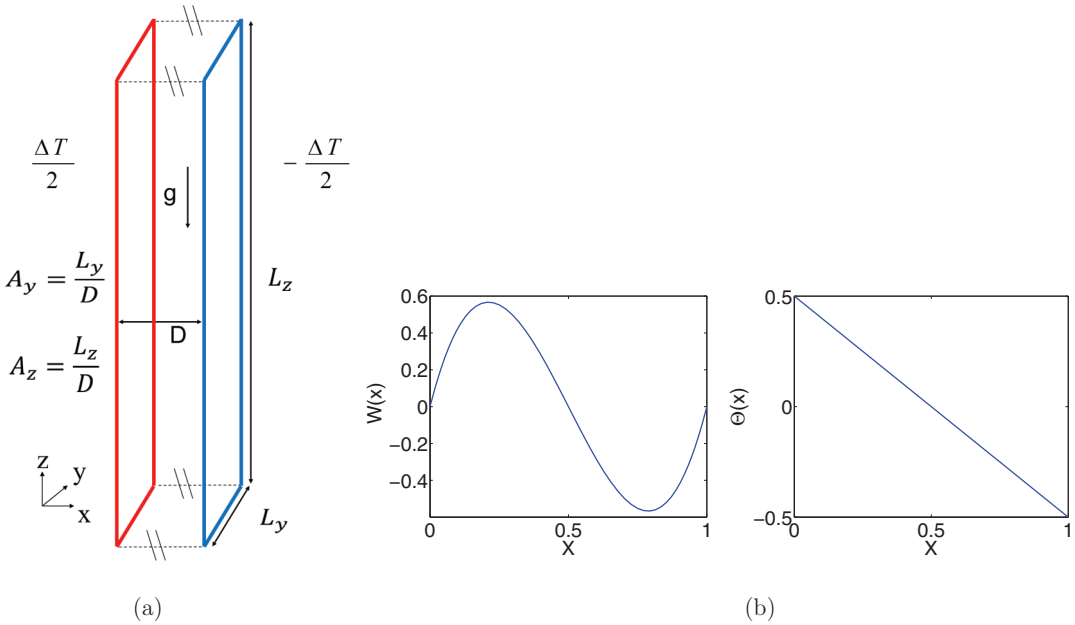

(a) (b)

FIG. 1. (Color online) (a) Study domain. (b) Base flow profiles for the temperature $\Theta(x)$ and vertical velocity $W(x)$.

and occasionally $A_z = 9$ and $A_z = 2.5$. The choice of these values is dictated by the critical wave number $k_c \sim 2\pi/2.5$ (see next section). The larger domain therefore could accomodate four structures.

A. Equations of motion

The flow is governed by the Navier-Stokes equations within the Boussinesq approximation. We choose the reference parameters to be $\frac{\kappa}{D}\sqrt{\mathrm{Ra}}$ for the velocity, D for the length, and ΔT for the temperature. The nondimensionalized equations then are

$$\vec{\nabla}\cdot\vec{u} = 0, \tag{1}$$

$$\frac{\partial\vec{u}}{\partial t} + \vec{u}\cdot\vec{\nabla}\vec{u} = -\vec{\nabla}\tilde{p} + \frac{\mathrm{Pr}}{\sqrt{\mathrm{Ra}}}\Delta\vec{u} + \mathrm{Pr}\,\tilde{\theta}\hat{z}, \tag{2}$$

$$\frac{\partial\tilde{\theta}}{\partial t} + \vec{u}\cdot\vec{\nabla}\tilde{\theta} = \frac{1}{\sqrt{\mathrm{Ra}}}\Delta\tilde{\theta}, \tag{3}$$

with Dirichlet boundary conditions at the plates,

$$\begin{aligned}&\vec{u}(0,y,z,t) = \vec{u}(1,y,z,t) = 0,\\ &\tilde{\theta}(0,y,z,t) = 0.5, \quad \tilde{\theta}(1,y,z,t) = -0.5,\end{aligned} \tag{4}$$

and periodic conditions in the y and z directions. Here t denotes time, $\vec{u} = (\tilde{u},\tilde{v},\tilde{w})$ is the velocity vector, $\tilde{p}$ is the pressure, and $\tilde{\theta}$ is the temperature.

The equations of motion (1)–(4) admit an analytic steady solution (U,V,W,Θ), the pure conduction state, which depends only on the x direction,

$$\begin{aligned}&U = 0; \quad V = 0;\\ &W(x) = \tfrac{1}{6}\sqrt{\mathrm{Ra}}\left[\left(x-\tfrac{1}{2}\right)^3 - \tfrac{1}{4}\left(x-\tfrac{1}{2}\right)\right];\\ &\Theta(x) = -\left(x-\tfrac{1}{2}\right).\end{aligned} \tag{5}$$

The solution Eq. (5) is represented in Fig. 1(b). The equations (1)–(4) admit an O(2) × O(2) symmetry. One O(2) symmetry corresponds to the translations in the transverse direction y and the reflection $y \to -y$, while the other corresponds to the translations in the vertical direction z and a reflection that combines centrosymmetry and Boussinesq symmetry: $(x,z,T) \to (1-x,-z,-T)$. The base flow possesses the same symmetry as the equations, since it is one-dimensional and antisymmetric with respect to the midplane $x = 0.5$.

B. Numerical configuration

The 2D simulations are carried out using a spectral DNS code [14] developed at the Laboratoire d'Informatique pour la Mécanique et les Sciences de l'Ingénieur (LIMSI). The code relies on a Chebyshev collocation discretization in the horizontal direction x and a Fourier discretization in the vertical direction z. The complete Navier-Stokes system is solved by inverting the Uzawa operator to ensure incompressibility. Over the range of Rayleigh numbers investigated, we choose 40 Chebyshev modes for the discretization in x and 160 Fourier modes in z for $A_z = 10$.

The 3D simulations are carried out with a multidomain spectral code [36] also developed at LIMSI. A Chebyshev-Fourier collocation method is used for spatial discretization. Incompressibility is enforced by the projection-correction method. The equations are integrated in time with a second-order mixed explicit-implicit scheme. The domain decomposition is carried out by the Schur complement and implemented with the MPI library. Some details about the numerical schemes are explained in Appendix A. In our study, the domain is decomposed into four subdomains in the z direction. A Chebyshev discretization is applied in directions x and z, while a Fourier discretization is used in the transverse direction y. For $A_y = 1$ and $A_z = 10$, we use 30 modes in the transverse direction y and 40 and 160 modes in the horizontal and vertical, x and z, directions, respectively. The initial condition is typically taken to be equal to the base flow.

Convergence of the spatial discretization in the 2D simulation has been established [14]. Convergence for the 3D code was checked by running the simulations using 45 Fourier modes in y and 60 and 240 Chebyshev modes in x and z, respectively. No significant difference was observed between the two spatial discretizations. Comparison of the 2D and 3D codes was carried out both below and slightly above the critical Rayleigh number. The difference between the flows was found to be within round-off error.

III. 2D THEORETICAL ANALYSIS OF THE FIRST BIFURCATION

A. Linear stability analysis

The base flow Eq. (5) is parallel and depends only on the x direction. The hypotheses of Squire's theorem are verified in this case, so the most unstable mode is expected to be 2D. We decompose the velocity and temperature into the base flow (U,W,Θ) and perturbations (u,w,θ) as

$$\tilde{u} = U + u, \quad \tilde{w} = W + w, \quad \tilde{\theta} = \Theta + \theta, \tag{6}$$

and take the curl of the momentum equations to eliminate the pressure term. Let ψ be the stream function for the perturbations, where $u = -\frac{\partial \psi}{\partial z}$, $w = \frac{\partial \psi}{\partial x}$. The equations of motion (1)–(4) lead to the 2D system of perturbations in x and z as

$$M\frac{\partial \phi}{\partial t} = L\phi + b(\phi,\phi), \tag{7}$$

with

$$\phi = \begin{bmatrix} \psi \\ \theta \end{bmatrix}; \quad b = \begin{bmatrix} b_\psi \\ b_\theta \end{bmatrix}; \quad M = \begin{bmatrix} \nabla^2 & 0 \\ 0 & 1 \end{bmatrix};$$
$$L = \begin{bmatrix} \frac{\mathrm{Pr}}{\sqrt{\mathrm{Ra}}}\nabla^4 - W\frac{\partial}{\partial z}\nabla^2 + \frac{\partial^2 W}{\partial x^2}\frac{\partial}{\partial z} & \mathrm{Pr}\frac{\partial}{\partial x} \\ \frac{\partial \Theta}{\partial x}\frac{\partial}{\partial z} & \frac{1}{\sqrt{\mathrm{Ra}}}\nabla^2 - W\frac{\partial}{\partial z} \end{bmatrix}, \tag{8}$$

where the nonlinear terms b_ψ and b_θ are bilinear forms and defined as

$$b_\psi(\phi_\alpha,\phi_\beta) = \left(\frac{\partial \psi_\alpha}{\partial z}\frac{\partial}{\partial x} - \frac{\partial \psi_\alpha}{\partial x}\frac{\partial}{\partial z}\right)\nabla^2\psi_\beta$$
$$b_\theta(\phi_\alpha,\phi_\beta) = \left(\frac{\partial \psi_\alpha}{\partial z}\frac{\partial}{\partial x} - \frac{\partial \psi_\alpha}{\partial x}\frac{\partial}{\partial z}\right)\theta_\beta. \tag{9}$$

The indices α and β will be used to designate the different orders of the solutions obtained in the multiscale analysis in the following subsection.

The associated boundary conditions are

$$\psi(x=0) = \psi(x=1) = 0, \tag{10}$$
$$\psi'(x=0) = \psi'(x=1) = 0, \tag{11}$$
$$\theta(x=0) = \theta(x=1) = 0, \tag{12}$$

where the prime symbol denotes partial differentiation with respect to x.

The linearized system is written as

$$M\frac{\partial \phi}{\partial t} = L\phi. \tag{13}$$

Seeking a normal-mode solution of the form $\phi = \hat{\phi}(x)e^{st+ikz}$, we obtain a generalized eigenvalue problem, $\hat{L}\hat{\phi} = s\hat{M}\hat{\phi}$.

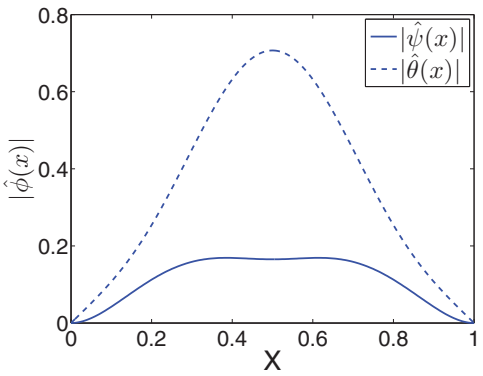

FIG. 2. (Color online) Norm of the most unstable mode $|\hat{\phi}(x)|$ ($|\hat{\psi}(x)|$,$|\hat{\theta}(x)|$) at k_c and Ra_c.

Solving the eigenvalue problem leads to a critical Rayleigh number $\mathrm{Ra}_c = 5708$ and a critical wave number $k_c = 2.81$, which agrees with the results of Bergholz [7] and Ruth [37]. The critical eigenvalue is purely real, and the modulus of the most unstable mode $|\hat{\phi}(x)|$ at the critical wave number k_c and Rayleigh number Ra_c is maximum in the core region, as shown in Fig. 2.

B. Weakly nonlinear analysis

We use a multiscale analysis to derive a Ginzburg-Landau equation for the flow around the first bifurcation. We introduce the asymptotic expansion of the perturbation to the base flow as

$$\phi = \epsilon\phi_1 + \epsilon^2\phi_2 + \epsilon^3\phi_3 + O(\epsilon^4). \tag{14}$$

We also define several time scales, $t_0 = t, t_1 = \epsilon t, t_2 = \epsilon^2 t$, and vertical length scales z, $z_0 = z, z_1 = \epsilon z$. We then expand all the operators in system (7) with respect to the new variables,

$$M = M_0 + \epsilon M_1 + \epsilon^2 M_2 + O(\epsilon^3), \tag{15}$$
$$L = L_0 + \epsilon L_1 + \epsilon^2 L_2 + O(\epsilon^3), \tag{16}$$
$$b = b_0 + \epsilon b_1 + \epsilon^2 b_2 + O(\epsilon^3), \tag{17}$$

where M_0, M_1, M_2, L_0, L_1, L_2, b_0, and b_1 are detailed in Appendix B.

The first-order perturbation $\epsilon\phi_1$ can be expressed as

$$\epsilon\phi_1 = \begin{bmatrix} \psi \\ \theta \end{bmatrix} = A(t_1,t_2,z_1)\begin{bmatrix} \hat{\psi}(x) \\ \hat{\theta}(x) \end{bmatrix} e^{st+ik_c z} + \text{c.c.}, \tag{18}$$

where $\hat{\psi},\hat{\theta}$ are the most unstable modes at the wave number k_c given by the linear stability analysis, A is the amplitude of the solution, and c.c. stands for complex conjugate.

Substituting these expansions into (7), and collecting the terms at different orders of ϵ, yields problems at different orders of ϵ. The problem at order ϵ coincides with the linear stability analysis. Collecting terms at order ϵ^2 and imposing a compatibility condition gives an expression for the group velocity C_g. Numerical evaluation of C_g yields a value of about 10^{-5}, which is close to the expected value of zero since the rolls are steady. The discrepancy is likely to be due to the discretization error.

1. Ginzburg-Landau equation

Collecting terms at order ϵ^3 and enforcing the solvability condition leads to a Ginzburg-Landau equation [38] for the amplitude A in the primitive variables,

$$\frac{\partial A}{\partial t} = \sigma(\mathrm{Ra} - \mathrm{Ra}_c)A + \gamma \frac{\partial^2 A}{\partial z^2} - lA^2A^*. \qquad (19)$$

Numerical evaluation of the coefficients σ, γ, l for the critical wave number $k_c = 2.81$ gives $\sigma = 7.67 \times 10^{-5}$, $\gamma = 0.112$, $l = 20.45$. The sign of l indicates that the bifurcation is supercritical. The amplitude of perturbations predicted by this Ginzburg-Landau equation will be compared with the DNS results discussed in the next section.

2. Absolute instability

The linearized Ginzburg-Landau equation takes the form

$$\frac{\partial A}{\partial t} = \sigma(\mathrm{Ra} - \mathrm{Ra}_c)A + \gamma \frac{\partial^2 A}{\partial z^2}. \qquad (20)$$

The introduction of a particular solution in the form of normal modes $A = \hat{A}e^{i(\beta z - \omega t)}$ into Eq. (20) results in the dispersion relation:

$$D(\omega,\beta,\mathrm{Ra}) = \sigma(\mathrm{Ra} - \mathrm{Ra}_c) + i\omega - \gamma\beta^2 = 0. \qquad (21)$$

It can be written in the form of a single temporal mode $\omega(\beta,\sigma,\mathrm{Ra}) = i[\sigma(\mathrm{Ra} - \mathrm{Ra}_c) - \gamma\beta^2]$, which has an equilibrium (β_0,ω_0), satisfying the conditions $\omega_0 = \omega(\beta_0)$ and $\frac{\partial\omega}{\partial\beta}(\beta_0) = 0$. The latter condition yields $\frac{\partial\omega}{\partial\beta}(\beta_0) = -2i\gamma\beta_0 = 0$. So $\beta_0 = 0$ and $\omega_0 = i\sigma(\mathrm{Ra} - \mathrm{Ra}_c)$. As $\omega_{0,i} = \sigma(\mathrm{Ra} - \mathrm{Ra}_c) > 0$, the disturbance grows with time at any fixed station in the laboratory frame, which corresponds to the absolute instability, in agreement with Tao and Zhuang's [39] results.

IV. NUMERICAL RESULTS

A. 2D DNS simulations

We first use a 2D simulation to study the development of instabilities in the flow. Results are summarized in Table I.

1. First bifurcation

As predicted by the linear stability analysis, the base flow bifurcates to four steady corotating rolls at $\mathrm{Ra}_c \sim 5708$. Although vertical invariance is broken, the solution still displays the symmetry D_4, consisting of translation by the height $A_z/4$ of each of the rolls. Invariance of the equations under z translations ensures that there exists a whole circle of solutions, corresponding to an arbitrary vertical translation of the rolls: The bifurcation is a circle pitchfork bifurcation.

The time evolution of the temperature measured at the point $(x = 0.0381,\ z = 5)$, located in the hot boundary layer, is plotted in Fig. 3(a). An enlargement of the same signal for the times $1500 < t < 2000$ is represented in logarithmic scale in Fig. 3(b). The temperature disturbance grows exponentially for $1500 < t < 1750$, which corresponds to the linear growth of the most unstable eigenmode and then increases at a slower rate for $t > 1750$ before the amplitude of the solution saturates. As was pointed out by Henderson and Barkley [40], this evolution shows that the coefficient of the cubic term in the normal form of the circle pitchfork bifurcation is negative, and, therefore, the bifurcation is supercritical, in agreement with the prediction of the Ginzburg-Landau model.

The steady amplitude A computed from the Ginzburg-Landau equation is compared with the amplitude of the velocity and temperature perturbations observed in the DNS for a domain which is as close as possible to the critical wavelength. The periodic height of the DNS was adjusted to $A_z = 9$, so it featured a wavelength of $\lambda = 2.25$ close to the critical wavelength $\lambda_c = 2.236$.

Figures 4(a) and 4(b) show that the agreement between the Ginzburg-Landau model and the DNS is very good for both the temperature and velocity up to $\mathrm{Ra} \sim 6300$ (about 10% above Ra_c).

2. Subsequent bifurcations

Figure 5 shows how the spatial organization of the flow varies with increasing Ra. Just above the critical Rayleigh number, the flow is characterized by four steady structures, as shown in Fig. 5(a) at $\mathrm{Ra} = 6000$. As Ra is increased past

TABLE I. Summary of bifurcations and associated flow structures and symmetries for the 2D simulations, $A_z = 10$.

Ra	Nature of bifurcation	Spatial features Number of structures	Spatial symmetry Temporal symmetry
$\mathrm{Ra} < \mathrm{Ra}_c = 5708$		1D base flow	O(2) Steady
$\mathrm{Ra}_c \leqslant \mathrm{Ra} \leqslant 13\,000$	Supercritical Circle pitchfork	Corotating rolls $n = 4$	D_4 Steady
$13\,500 \leqslant \mathrm{Ra} \leqslant 15\,300$	Supercritical Hopf	Corotating rolls $n = 3$	No symmetry Periodic
$15\,400 \leqslant \mathrm{Ra} \leqslant 15\,600$	 Unknown	Corotating rolls $n = 3$	No symmetry Quasiperiodic
$15\,700 \leqslant \mathrm{Ra} \leqslant 17\,000$	 Unknown	Corotating rolls $n = 3$	No symmetry "Chaotic"
$18\,000 \leqslant \mathrm{Ra} \leqslant 21\,000$	 Unknown	Corotating rolls $n = 2$	No symmetry Steady

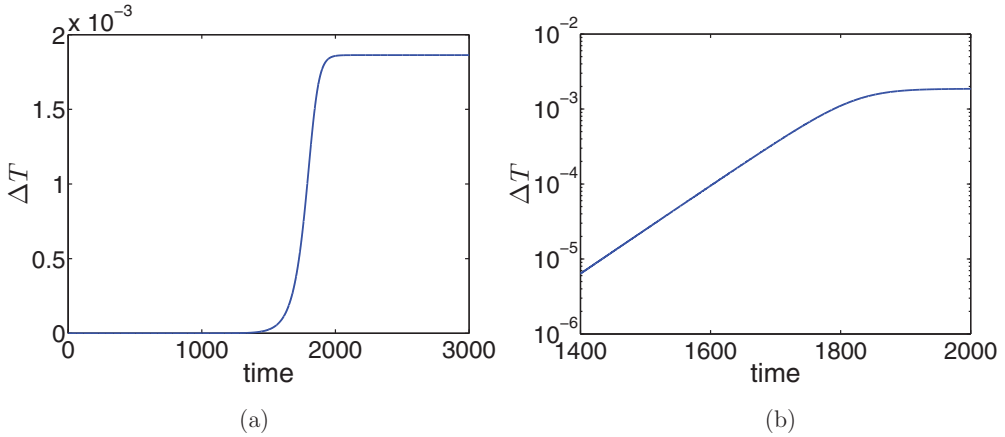

(a) (b)

FIG. 3. (Color online) (a) Time series of temperature perturbation at point (0.0381, 5) in the boundary layer near the hot wall at Ra = 6000. (b) An enlargement of (a) for $1500 < t < 2000$ on a logarithmic scale.

the value of Ra = 13 500, the four steady rolls merge into three rolls which oscillate in time, as shown in Fig. 5(b). At still higher Rayleigh numbers Ra $\geqslant$ 18 000, only two rolls of unequal size are observed, as shown in Fig. 5(d).

The temporal spectrum of the vertical velocity at the point ($x = 0.0381$, $z = 0.683$) is shown in Fig. 6(a) and is characterized by a main frequency (with harmonics) of $f_1 = 0.032$. When 15 000 $\leqslant$ Ra $\leqslant$ 16 000, the flow still consists of three oscillatory rolls, but the temporal evolution of the flow becomes more complex. When Ra is increased to Ra = 15 500, the flow becomes quasiperiodic with the appearance of a second, much lower, frequency, $f_2 = 0.0031$ [Fig. 6(b)]. When Ra = 16 000, the peaks around the main frequency f_1 and f_2 broaden [see Fig. 6(c)], corresponding to seemingly chaotic behavior. The chaotic behavior subsides beyond Ra = 18 000, as the flow spatial pattern is modified: There seems to be a competition between the onset of purely temporal chaos in a specific flow pattern and the development of spatial instabilities at short wave numbers. Up to Ra = 21 000, which was the highest Rayleigh number considered, the flow remains steady with a robust two-roll pattern.

B. 3D DNS results: First bifurcation

We first check that the base flow remains stable with respect to any perturbation when Ra < Ra_c. As expected, the first bifurcation observed in the DNS occurs at Ra_c around 5800 and is characterized by the appearance of four 2D steady corotating rolls which are represented in Fig. 7. As mentioned above, the vertical translation invariance is replaced with a D_4 symmetry, and the centro-Boussinesq symmetry is conserved.

C. Second bifurcation: 3D steady structures

When Ra > Ra_{c2}, the four-roll solution becomes unstable in the transverse direction, and a steady 3D pattern, shown in Fig. 8, appears through a second bifurcation, as was also found by Nagata and Busse [23] and Clever and Busse [24]. Since the transition breaks the y-translation invariance, this new bifurcation is also a circle pitchfork bifurcation. From the analysis of a time series similar to that of Fig. 3, we conclude that this bifurcation is supercritical.

The threshold Ra_{c2} can be obtained by linearizing the equations of motion around the 2D steady solution and

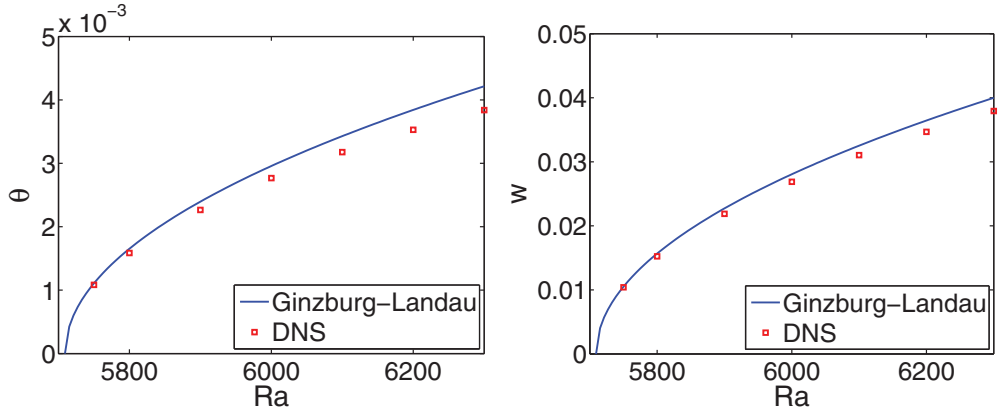

(a) (b)

FIG. 4. (Color online) Comparison of the maximum amplitudes observed in the 2D DNS at $x = 0.0381$ with the Ginzburg-Landau equation prediction: (a) temperature and (b) vertical velocity.

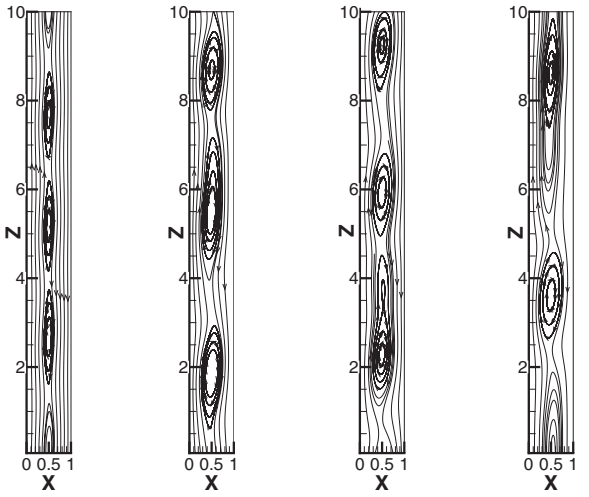

(a) Ra=6000 (b) Ra=13 500 (c) Ra=15 000 (d) Ra=18 000

FIG. 5. 2D flow streamlines at different Ra. (a) Four steady corotating rolls; [(b) and (c)] three oscillating rolls; (d) two steady rolls.

integrating a small perturbation in time for different values of Ra. The growth rate of these perturbations, which is equal to the most unstable eigenvalue, is found to increase quasilinearly with Ra. The critical Rayleigh number Ra_{c2} obtained by linear extrapolation of the plot is around 9980, which is within 2% of the value Ra $\sim$ 10 100 observed in the DNS.

The steady 3D solution retains some of the symmetry of the 2D solutions, namely the reflection in y and translation by $A_z/4$ in z, but the translation symmetry in y and the centro-Boussinesq symmetry are replaced with the single discrete symmetry

$$(x,y,z,T) \to (1-x, y+0.5, A_z - z, -T). \qquad (22)$$

The 2D solution, which was $\mathrm{O}(2) \times D_4$ symmetric, has bifurcated to a 3D solution with $D_1 \times D_4$ symmetry.

This can be seen in Fig. 9, which shows temperature contours and streamlines on three planes parallel to the plates. The field obeys the symmetry (22), as can be seen by comparing Figs. 9(a) with 9(c) or Figs. 9(d) with 9(f). The upwind motion on the plane $x = 0.0381$ along the hot wall [Fig. 9(d)] and the downwind motion on the plane $x = 0.9619$ along the cold wall [Fig. 9(f)] are captured. On the midplane, the streamline plot of Fig. 9(e) shows two large and two small

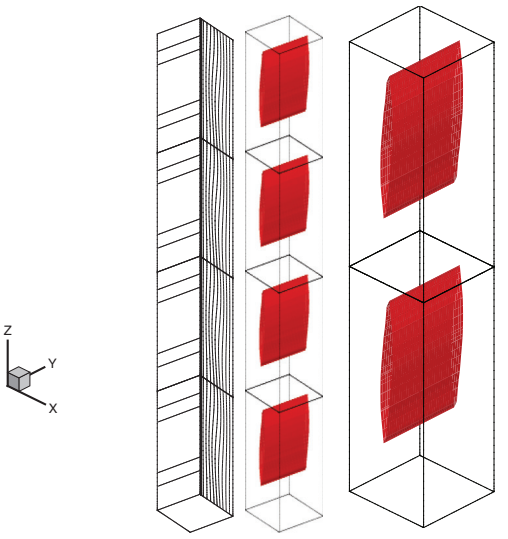

(a) (b) (c)

FIG. 7. (Color online) Flow structure at Ra = 6000. (a) Isocontours of the temperature on the two selected vertical plates $x = 0.0245$ and $y = 0.9677$, (b) isosurface of transverse vorticity $\Omega_y = 3.1$, and (c) enlargement of the upper half of the domain in (b).

secondary counter-rotating vortices. Since the flow is invariant under translation by $A_z/4$, we restrict our analysis to the upper half of the domain in the rest of this section.

Figure 10 shows isosurfaces of the vorticity components Ω_y, Ω_x, Ω_z along with the Q criterion [41]. The Q criterion is defined as

$$Q = \tfrac{1}{2}(\Omega_i \Omega_i - E_{ij} E_{ij}),$$

where E_{ij} is the rate of strain tensor $\frac{1}{2}(\frac{\partial u_i}{\partial x_j} + \frac{\partial u_j}{\partial x_i})$ and therefore provides a measure of the vortices. Comparison of Figs. 10(a) and 10(d) show that most of the vorticity is transverse and is organized into the corotating convection rolls corresponding to the most linearly unstable mode.

Examination of the horizontal vorticity (Ω_x) plots in Fig. 10(b) confirms that the flow is characterized by two counter-rotating vortices, which are inclined 45° with respect to both the horizontal and the vertical planes. As shown in Fig. 10(d), these secondary circulations link the primary rolls and are to some extent reminiscent of the three-dimensional braids connecting the primary vortices observed in shear layers

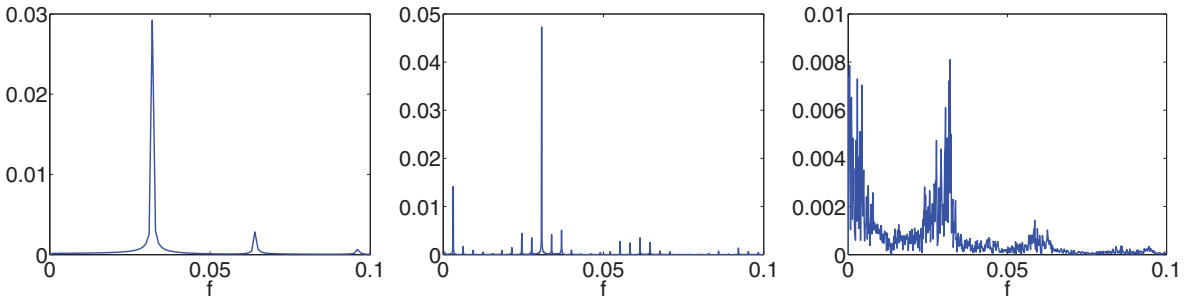

(a) Ra = 15 000 (b) Ra = 15 500 (c) Ra = 16 000

FIG. 6. (Color online) Temporal Fourier spectrum of the vertical velocity at the point (0.0381, 0.683) in the boundary layer near the hot wall in 2D simulations for different Rayleigh numbers.

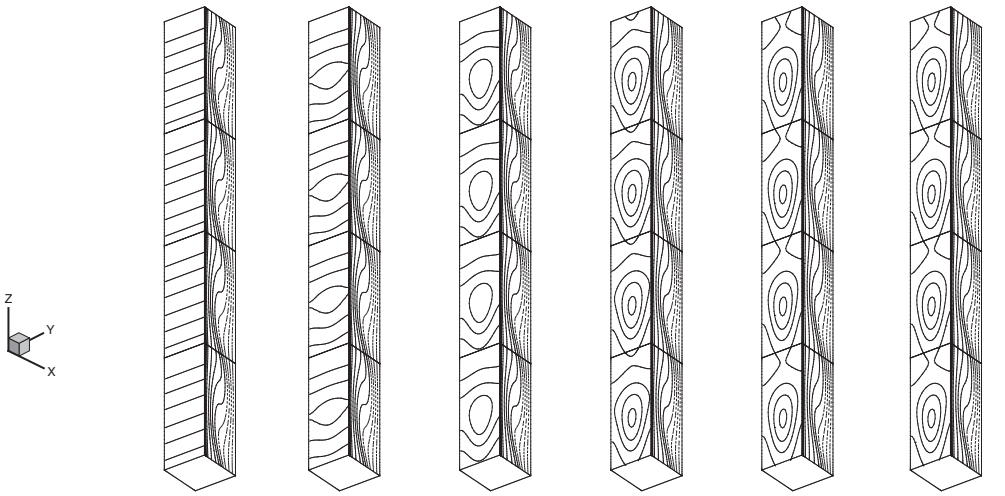

(a) t=500 (b) t=1040 (c) t=1090 (d) t=1120 (e) t=1170 (f) t=2000

FIG. 8. Flow structure at Ra = 11000. [(a)–(f)] Temperature isocontours on the two planes $x = 0.0245$ (next to the hot wall) and $y = 0.9677$ (perpendicular to sidewalls) at times as indicated.

before vortex pairings [42]. In addition, Fig. 10(c) shows the presence of additional counter-rotating vortices within the primary convection rolls. These vortices are about half the height of the larger secondary vortices, and their orientation is opposite to that of the larger secondary vortices. They are predominantly aligned with the vertical direction z.

In summary, the flow structure for the 3D pattern consists of (1) principal vertical corotating rolls predominantly aligned in the transversal direction y, (2) large secondary counter-rotating vortices or braids linking up the primary rolls, which are inclined about 45° with respect to the horizontal and the vertical planes, and (3) two vertical, short counter-rotating vortices located within the principal rolls.

D. Third bifurcation: 3D time-periodic flow

The 3D pattern remains stable up to a value of $\mathrm{Ra} < \mathrm{Ra}_{c3}$. For $\mathrm{Ra}_{c3} < \mathrm{Ra} < 12\,000$, the 3D pattern becomes time dependent.

1. Local analysis

The time series of the temperature at a point located in the hot boundary layer is plotted in Fig. 11(a). Figure 11(b) shows that it corresponds to a periodic signal of frequency $f_1 = 0.036$, very close to the basic frequency $f_1^{2D} = 0.032$ found in the 2D simulations at a slightly higher Rayleigh number.

During this periodic regime, we observe that the oscillation frequency f_1 is nearly constant as the Rayleigh number

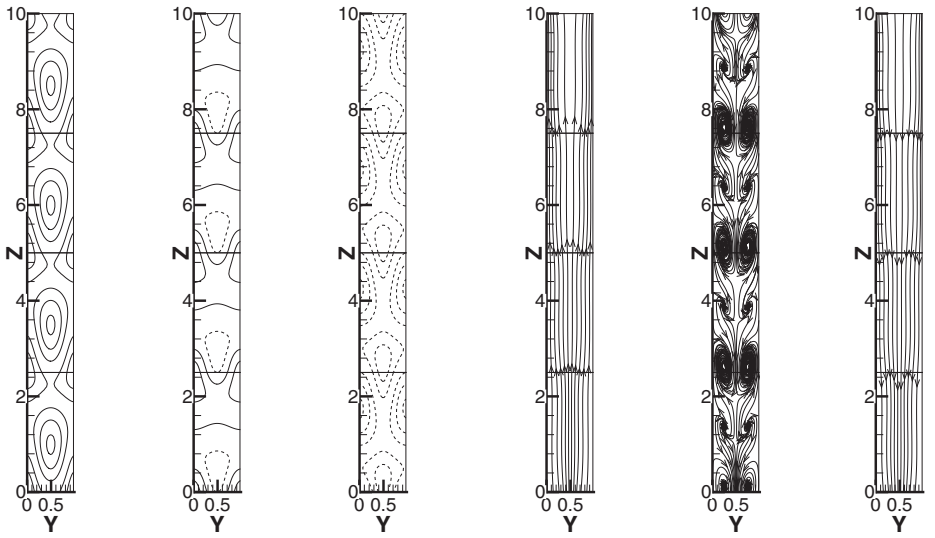

(a) $x = 0.0381$ (b) $x = 0.5$ (c) $x = 0.9619$ (d) $x = 0.0381$ (e) $x = 0.5$ (f) $x = 0.9619$

FIG. 9. [(a)–(c)] Temperature isocontours on two planes which are symmetric with respect to the vertical midplane ($x = 0.5$); [(d)–(f)] streamlines on the same three vertical planes at Ra = 11 000.

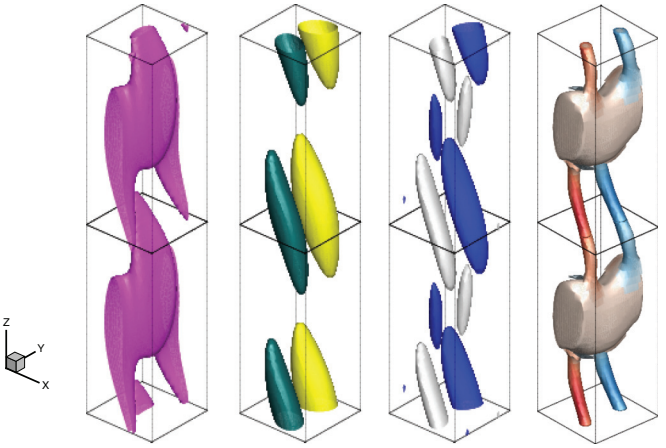

(a) $\Omega_y = 3$ (b) $\Omega_x = \pm 1$ (c) $\Omega_z = \pm 0.5$ (d) $Q = 0.12$

FIG. 10. (Color online) Vorticity isosurfaces at Ra = 11 000.

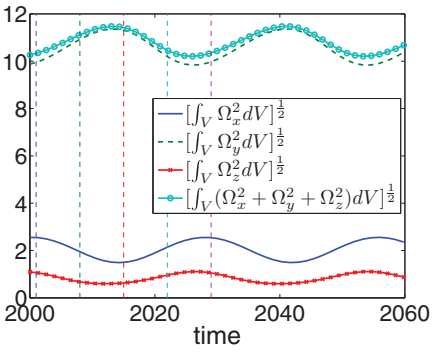

FIG. 12. (Color online) Temporal evolution of horizontal vorticity intensity $[\int_V \Omega_x^2 dV]^{\frac{1}{2}}$, transverse vorticity intensity $[\int_V \Omega_y^2 dV]^{\frac{1}{2}}$, and vertical vorticity intensity $[\int_V \Omega_z^2 dV]^{\frac{1}{2}}$ at Ra = 11 500.

increases above its bifurcation value, while the square of the oscillation amplitude increases linearly with Ra. This is consistent with a Hopf bifurcation. The critical Rayleigh number Ra_{c3} evaluated by the linear extrapolation of the oscillation amplitude as a function of Ra is around $\mathrm{Ra}_{c3} = 11\,270$, in excellent agreement with results from the DNS observations.

2. *Global enstrophy budgets*

Some insight into the dynamics of the flow can be given by enstrophy, which gives a measure of rotational effects in the flow. The total contribution to the enstrophy of each vorticity component $[\int_V \Omega_j^2 dV]^{1/2}$ was computed, where $j = x, y, z$ and Ω_j is the j-th component of the vorticity. As we can see from Fig. 12, most of the enstrophy is contained in the transverse contribution $[\int_V \Omega_y^2 dV]^{\frac{1}{2}}$. Both the horizontal and vertical contributions oscillate essentially in phase opposition with the transverse contribution.

A physical interpretation of this plot is given in Fig. 13. The flow structures are similar to the steady ones observed in the previous regime (and therefore retain the same spatial symmetry), but they now pulse periodically. When the primary rolls are strongest, the secondary vortices disappear. At this moment, the flow is mostly two-dimensional [Fig. 13(c)]. In contrast, when the secondary vortices reach their maximum intensities, the primary rolls bend in the transverse direction; the strongly 3D flow can be seen in Fig. 13(e).

We note that the frequency f of the oscillation is very close to the natural frequency of the mixing layer $f_n \sim 0.032$ [42], when it is nondimensionalized with the distance between the plates and the maximum velocity difference observed in the base flow.

To better understand the origin of the oscillations, we consider the vorticity equation:

$$\frac{\partial \Omega_i}{\partial t} + u_j \frac{\partial \Omega_i}{\partial x_j} - \Omega_j \frac{\partial u_i}{\partial x_j} = \frac{\mathrm{Pr}}{\sqrt{\mathrm{Ra}}} \frac{\partial^2 \Omega_i}{\partial x_j \partial x_j} - \mathrm{Pr}\, \varepsilon_{ijk} \frac{\partial \theta \delta_{j3}}{\partial x_k}. \tag{23}$$

If we multiply equation (23) by $2\Omega_i$, we obtain

$$\frac{\partial \Omega_i^2}{\partial t} + u_j \frac{\partial \Omega_i^2}{\partial x_j} = 2\Omega_i \Omega_j \frac{\partial u_i}{\partial x_j} + 2\frac{\mathrm{Pr}}{\sqrt{\mathrm{Ra}}} \Omega_i \frac{\partial^2 \Omega_i}{\partial x_j \partial x_j} - 2\Omega_i \mathrm{Pr}\, \varepsilon_{ijk} \frac{\partial \theta \delta_{j3}}{\partial x_k}. \tag{24}$$

(We sum over j and k but not over i, and ε is the permutation symbol and δ is the Kronecker symbol.) The terms on the

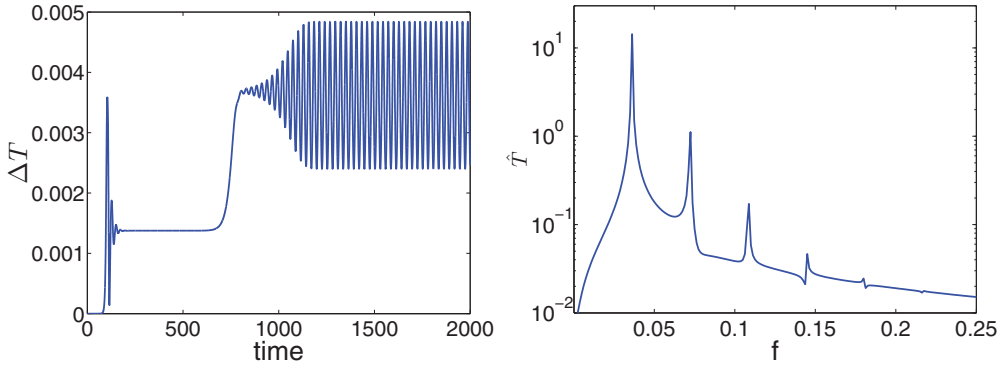

(a) (b)

FIG. 11. (Color online) (a) Time series of temperature perturbation at the point (0.0381, 0.097, 5) in the boundary layer near the hot wall, Ra = 11 500. (b) Temporal Fourier spectrum of the periodic portion $t \in [1200, 2000]$ of the signal (a).

right-hand side of the equations correspond to the production—or destruction—of Ω_i^2 through three different mechanisms: (i) vortex stretching, which is tilting and stretching of vorticity components by the velocity field, (ii) friction, i.e., the action of viscosity (which we will also refer to as diffusion), and (iii) buoyancy. Summing over i (i.e., using the tensor notation for i) yields the enstrophy equation. We choose instead to integrate the equation corresponding to each component over the domain. One can check that the transport term (second term on the left-hand side) disappears, so we are left with the following equations for each vorticity component:

$$\begin{bmatrix} \int_V \frac{\partial \Omega_x^2}{\partial t} dV \\ \int_V \frac{\partial \Omega_y^2}{\partial t} dV \\ \int_V \frac{\partial \Omega_z^2}{\partial t} dV \end{bmatrix} = \begin{bmatrix} \int_V \left(2\Omega_x(\vec{\Omega}\cdot\vec{\nabla}u) + 2\frac{\mathrm{Pr}}{\sqrt{\mathrm{Ra}}}\Omega_x\nabla^2\Omega_x + 2\mathrm{Pr}\Omega_x\frac{\partial\theta}{\partial y}\right)dV \\ \int_V \left(2\Omega_y(\vec{\Omega}\cdot\vec{\nabla}v) + 2\frac{\mathrm{Pr}}{\sqrt{\mathrm{Ra}}}\Omega_y\nabla^2\Omega_y - 2\mathrm{Pr}\Omega_y\frac{\partial\theta}{\partial x}\right)dV \\ \int_V \left(2\Omega_z(\vec{\Omega}\cdot\vec{\nabla}w) + 2\frac{\mathrm{Pr}}{\sqrt{\mathrm{Ra}}}\Omega_z\nabla^2\Omega_z\right)dV \end{bmatrix}. \quad (25)$$

Figures 14 to 16 present the global evolution and spatial distribution of the three terms on the right-hand side of Eq. (39) for each vorticity component. The balance in the horizontal direction can be seen in Fig. 14(a). The vortex-stretching term and the buoyancy term are both source terms and oscillate with a small phase shift, while the friction term is negative and oscillates in phase opposition with the other two contributions. As the intensity of the friction is not quite compensated by the effect of vortex stretching and buoyancy, this results in limited oscillations of the horizontal vorticity rms $[\int_V \Omega_x^2 dV]^{\frac{1}{2}}$. The spatial distribution of the contributions due to vortex stretching, viscous effects, and buoyancy is represented in Figs. 14(b)–14(d) on a plane orthogonal to the plates. The plane was chosen in order to provide a relevant cross section of one of the vorticity braids, i.e., the secondary counter-rotating vortices. The vortex-stretching and buoyancy terms are both positive everywhere [Figs. 14(b) and 14(d)], while the friction term is negative [Fig. 14(c)]. All terms reach their maximum over the portion of space occupied by the counter-rotating vortices.

Figure 15(a) represents the different contributions to equation (25) for the transverse component. All three terms oscillate essentially in phase (with phase shifts of about $1/8$ and $1/12$ of the time period), which is responsible for the strong oscillation observed in the principal rolls. The vortex-stretching term is always positive, as can be expected. Perhaps a more surprising result is that friction is now a source term for the transverse vorticity, while buoyancy constitutes a sink for it. Since the temperature gradient is always negative and the principal rolls are associated with positive transverse vorticity Ω_y, one would expect a positive value for $-2\mathrm{Pr}\,\Omega_y\frac{\partial\theta}{\partial x}$. To understand this discrepancy, we examined the spatial distribution of the different contributions, which can be seen in Figs. 15(b)–15(d) for the symmetry plane $y = 0.5$. The effect of vortex stretching was essentially positive, as could be expected [Fig. 15(b)]. Over the portion of space covered by the principal vortices, the contribution of the buoyancy was also found to be positive [Fig. 15(d)], but strongly negative values were observed very close to the wall in the boundary layer, which is where the temperature gradient is significant. The situation was reversed for friction effects: strongly positive values were found very close to the walls. This reflects the fact that transverse vorticity is indeed generated at the walls through friction, while buoyancy works against the velocity gradient in the wall layer.

Figure 16(a) represents the relative contributions of vortex stretching and friction to the oscillations of the vertical component of the enstrophy. These oscillations are limited, since the positive effect of vortex stretching is almost exactly compensated by frictional effects (buoyancy does not appear in the equations). As can be seen in Figs. 16(b) and 16(c), both friction and vortex-stretching contributions are maximal at the location of the counter-rotating vortices.

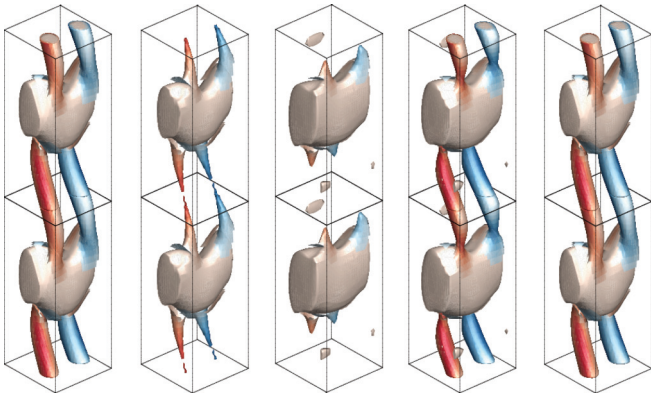

(a) $t = 2001$ (b) $t = 2008$ (c) $t = 2015$ (d) $t = 2022$ (e) $t = 2029$

FIG. 13. (Color online) Q criterion isosurface $Q = 0.12$ at selected times (corresponding vertical lines in Fig. 12) spanning one temporal oscillation, $\mathrm{Ra} = 11\,500$.

E. 3D subsequent bifurcations

1. Period-doubling bifurcations

Case $A_z = 10$. When $12\,100 \leqslant \mathrm{Ra} \leqslant 12\,200$, the temporal evolution of the 3D pattern becomes more complex. At $\mathrm{Ra} = 12\,200$, the time series of the temperature at a point located in the boundary layer presents subharmonic oscillations for $t \in [800, 2200]$ before becoming quite irregular, as shown in Fig. 17(a). The Fourier spectrum of the temperature [Fig. 17(b)] shows that the largest amplitude is located at the frequency $f_1 = 0.035$, which is close to the frequency identified in the previous periodic regime at a slightly lower Rayleigh number (see Sec. IV D1), while the second-largest amplitude corresponds to the frequency $f_{1/2} = 0.0175 = f_1/2$.

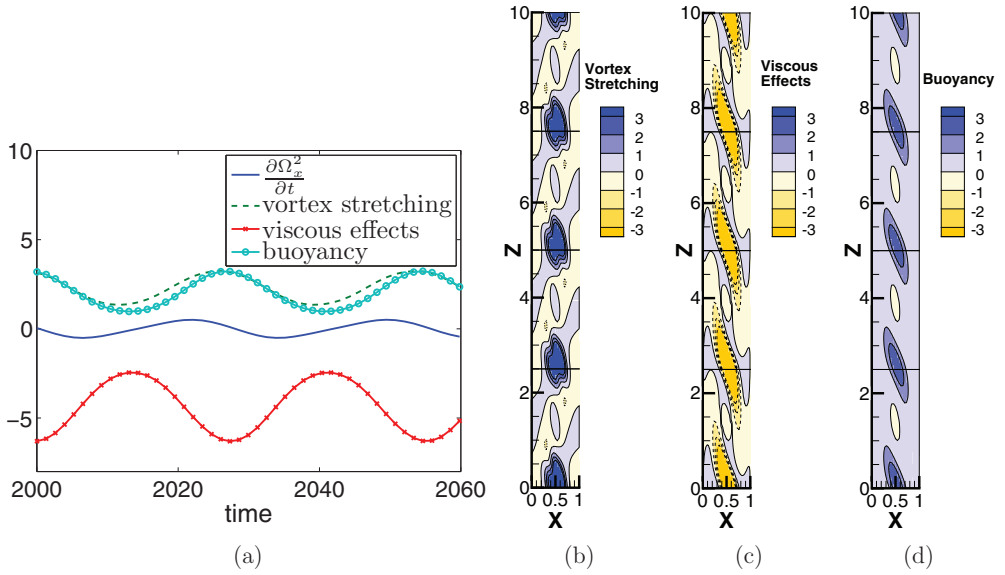

FIG. 14. (Color online) (a) Temporal evolution of the different terms in Eq. (25) for the x component: time derivative of the transverse vorticity $\int_V \frac{\partial\Omega_x^2}{\partial t} dV$, vortex-stretching contribution $\int_V 2\Omega_x(\vec{\Omega}\cdot\vec{\nabla}w)dV$, and friction effects $\int_V \frac{\mathrm{Pr}}{\sqrt{\mathrm{Ra}}}\Omega_x\nabla^2\Omega_x dV$; [(b)–(d)] spatial distribution of (b) the vortex-stretching contribution $2\Omega_x(\vec{\Omega}\cdot\vec{\nabla}u)$, (c) the friction contribution $\frac{\mathrm{Pr}}{\sqrt{\mathrm{Ra}}}\Omega_x\nabla^2\Omega_x$, and (d) the buoyancy contribution $2\mathrm{Pr}\,\Omega_x\frac{\partial\theta}{\partial y}$ on the vertical plane $y = 0.2903$ at $t = 2000$, $\mathrm{Ra} = 11\,500$.

The topology of the flow consists of four 3D structures which are similar to those found in the monoperiodic regime at $\mathrm{Ra} = 11\,500$ (Sec. IV D1). The intensities of the transverse rolls and that of the braids oscillate out of phase, with a temporal modulation equal to twice the basic period.

Case $A_z = 2.5$. Period doubling persists when the height was set to $A_z = 2.5$ instead of $A_z = 10$. As Ra increases, we observe for $A_z = 2.5$ a succession of period-doubling bifurcations as illustrated by phase portraits in Fig. 18. At $\mathrm{Ra} = 12\,000$, the singly periodic regime is characterized by one cycle in the phase portrait [Fig. 18(a)]. For $\mathrm{Ra} \in [12\,100, 12\,200]$, a period-2 cycle is observed in Fig. 18(b). At $\mathrm{Ra} = 12\,300$, we observe a 4-cycle in the phase portraits and then at $\mathrm{Ra} = 12\,310$ an 8-cycle and at $\mathrm{Ra} = 12\,320$ a 16-cycle [Figs. 18(c)–18(e)].

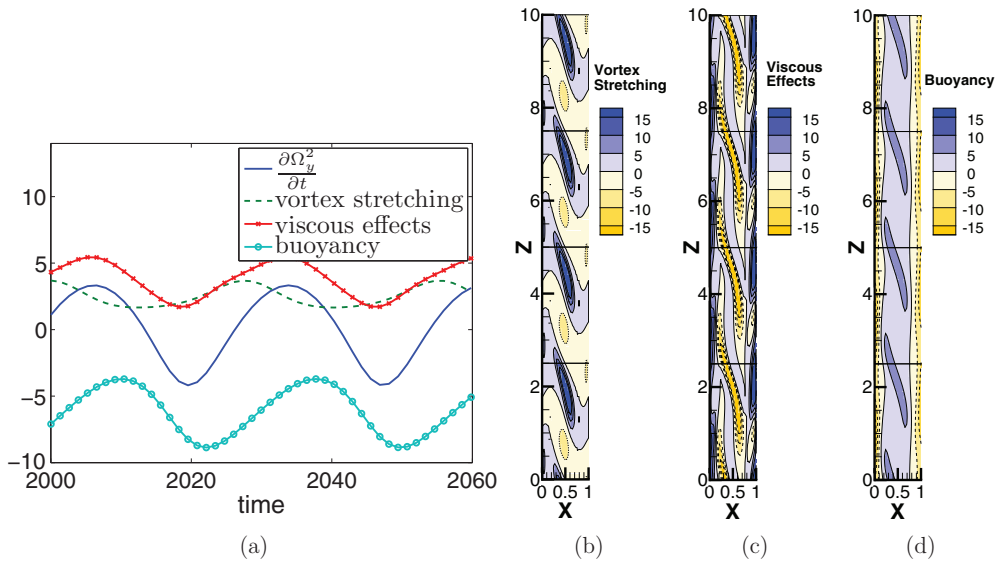

FIG. 15. (Color online) (a) Temporal evolution of the different terms in equation (25) for the y component: time derivative of the transverse vorticity $\int_V \frac{\partial\Omega_y^2}{\partial t} dV$, vortex-stretching contribution $\int_V 2\Omega_y(\vec{\Omega}\cdot\vec{\nabla}w)dV$, and friction effects $\int_V \frac{\mathrm{Pr}}{\sqrt{\mathrm{Ra}}}\Omega_y\nabla^2\Omega_y\, dV$; [(b)–(d)] spatial distribution of (b) the vortex-stretching contribution $2\Omega_y(\vec{\Omega}\cdot\vec{\nabla}v)$, (c) the friction effects $\frac{\mathrm{Pr}}{\sqrt{\mathrm{Ra}}}\Omega_y\nabla^2\Omega_y$, and (d) the buoyancy contribution $-2\mathrm{Pr}\,\Omega_y\frac{\partial\theta}{\partial x}$ on the vertical plane $y = 0.5$ at $t = 2000$, $\mathrm{Ra} = 11\,500$.

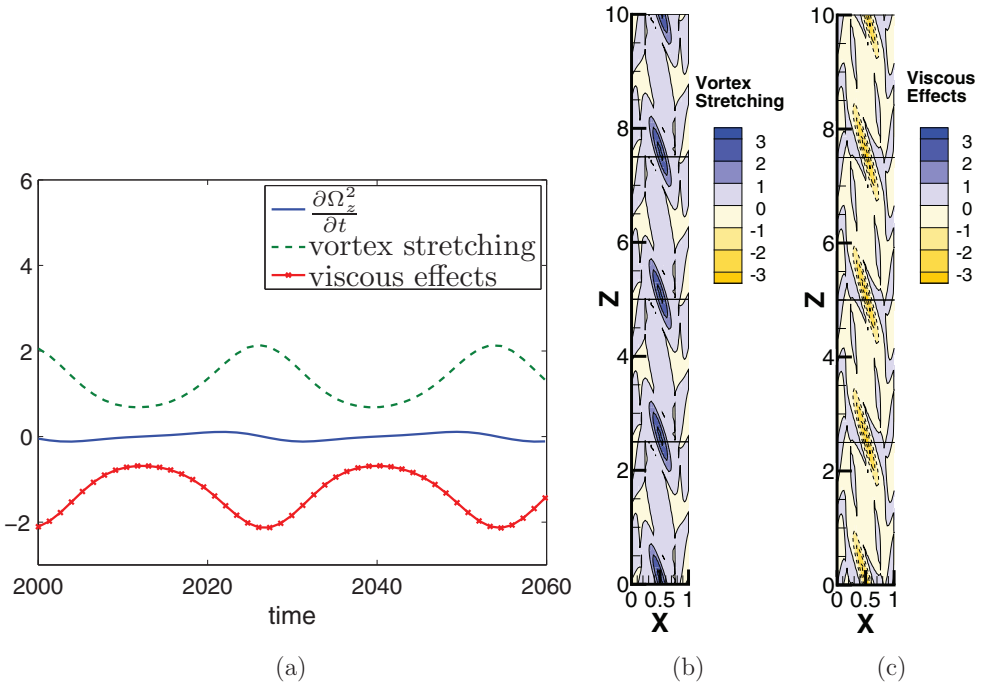

FIG. 16. (Color online) (a) Temporal evolution of the different terms in Eq. (25) for the z component: time derivative of the vertical vorticity $\int_V \frac{\partial \Omega_z^2}{\partial t} dV$, vortex-stretching contribution $\int_V 2\Omega_z(\vec{\Omega}\cdot\vec{\nabla}w)dV$, and friction effects $\int_V \frac{\mathrm{Pr}}{\sqrt{\mathrm{Ra}}}\Omega_z\nabla^2\Omega_z\, dV$; [(b) and (c)] spatial distributions of (b) the vortex-stretching contribution $2\Omega_z(\vec{\Omega}\cdot\vec{\nabla}w)$ and (c) the friction contribution $\frac{\mathrm{Pr}}{\sqrt{\mathrm{Ra}}}\Omega_z\nabla^2\Omega_z$ at the vertical plane $y = 0.2903$ (same as in Fig. 14) at $t = 2000$, $\mathrm{Ra} = 11\,500$.

At $\mathrm{Ra} = 12\,400$, there is no longer evidence of periodicity as the trajectory fills out the space in a seemingly chaotic fashion [Fig. 18(f)]. Similar sequences of period-doubling bifurcations have been observed in the experimental transition to chaos in Rayleigh-Bénard convection. Maurer and Libchaber [43] observed the appearance of a first frequency f_1', followed by a second frequency f_2'. For higher values of the Rayleigh number, phase locking between the frequencies was observed. The transition to turbulence was then triggered by the generation of the frequencies $f_2'/2$, $f_2'/4$, and so forth. A similar scenario was found in the experiments of Giglio, Musazzi, and Perini [44], where a reproducible sequence of period-doubling bifurcations up to $f_1'/16$ was observed.

As the Ra is further increased beyond $\mathrm{Ra} = 12\,550$, intermittency is observed in Fig. 19(a). The 3D structures keep pulsating chaotically, but, at random times, the primary rolls disappear entirely and reform at a different location, which is separated from the original location by half a wavelength, as shown in Figs. 19(b) and 19(c). This behavior suggests the existence of a heteroclinic connection between two chaotic attractors, which are diametrically located on the O(2) × O(2) invariant torus of chaotic solutions. The jump from one pulsating structure to another appears to take place only in the vertical direction (the system is severely constrained in the spanwise direction). Structurally stable heteroclinic connections between fixed points or periodic solutions have

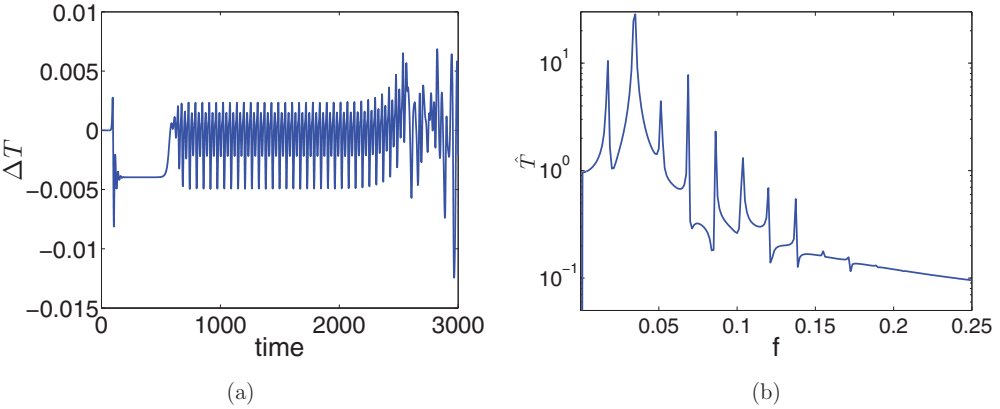

FIG. 17. (Color online) (a) Time series of temperature perturbation at the point (0.0381, 0.097, 5) in the boundary layer near the hot wall, $\mathrm{Ra} = 12\,200$, $A_z = 10$. (b) Temporal Fourier spectrum of the subharmonic portion in the time interval $t \in [1200, 2000]$.

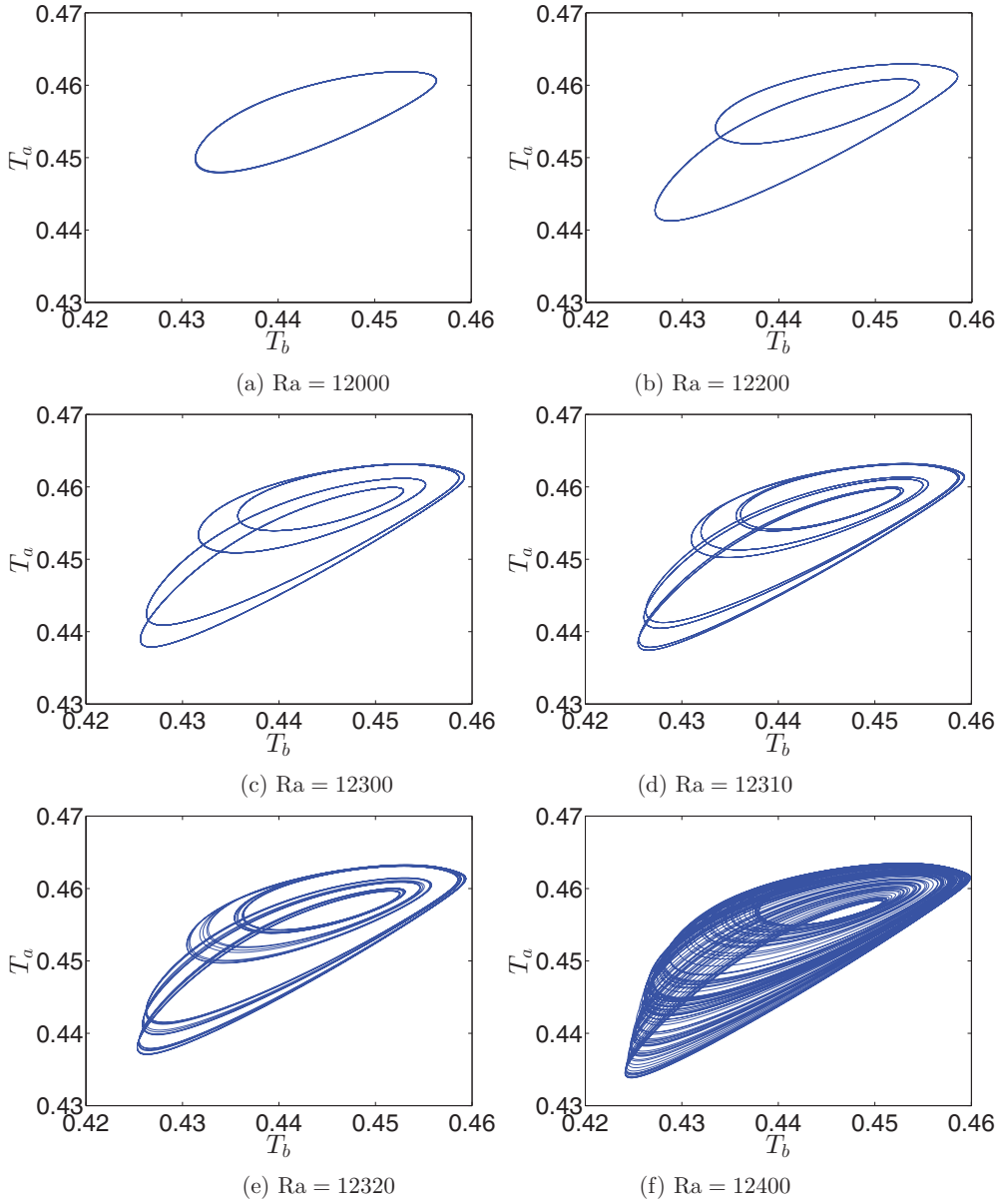

(a) Ra = 12000 (b) Ra = 12200

(c) Ra = 12300 (d) Ra = 12310

(e) Ra = 12320 (f) Ra = 12400

FIG. 18. (Color online) Phase portraits at different Ra, $A_z = 2.5$. Abscissa: T_a temperature mesured at the point (0.038, 0.097, 0.983); ordinate: T_b temperature measured at the point (0.038, 0.903, 0.983).

been shown to exist in systems with O(2) symmetry [45,46]. We are not aware of corresponding theoretical results for chaotic attractors.

2. Development of a spatial instability in the large domain $A_z = 10$

For Ra $\geqslant$ 12 200, we observed irregular oscillations in Fig. 17 for large times $t > 2200$. This corresponds to a drastic change in the spatial organization of the flow, as shown in Fig. 20. One of the structures is weakened and then disappears so at large times $t > 2200$, the pattern observed typically consists of three structures, as can be seen in Figs. 20(b), 20(c), and 20(f). However, four structures can still be found intermittently [Figs. 20(a), 20(d), and 20(e)].

The spatial organization of the flow can be described by the 1D vertical Fourier transform $\hat{T}(0,k)$ of the x-averaged temperature on the vertical plane $y = 0.5$. The temporal evolution of the spectral coefficients $|\hat{T}(0,k)|^2$ for the modes $k = 3,4$ is shown in Figs. 21(a) and 21(b). The mode $k = 4$ dominates when $700 < t < 2000$, and then for $t \in [4000,6000]$ the mode $k = 3$ dominates for most of the time, except around the times $t \sim 5040$ and $t \sim 5950$, where the mode $k = 4$ becomes dominant again. Due to the long integration times, we were not able to determine whether the spatial intermittency was a transient or a persistent feature of the flow.

A simulation was performed at Ra = 12 000 from an initial condition consisting of a instantaneous field at Ra = 12 200 characterized by a three-structure pattern. The flow settled

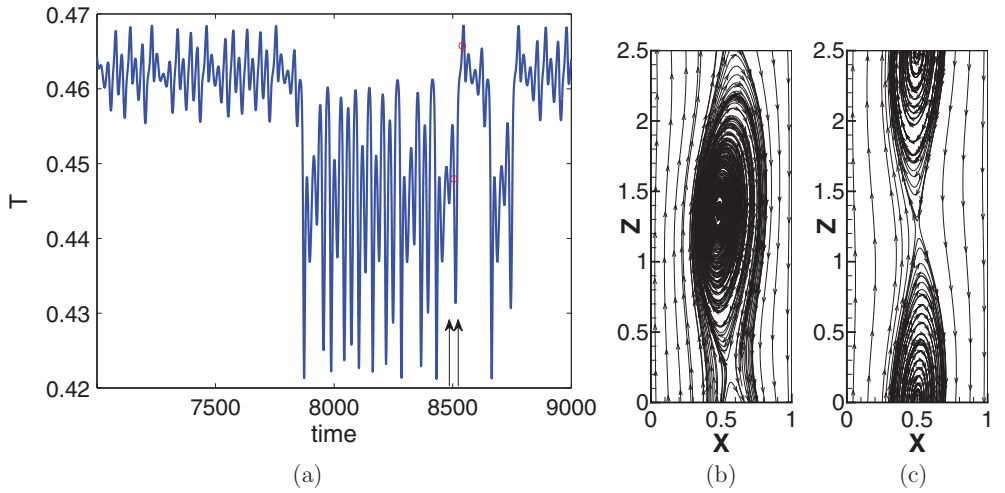

FIG. 19. (Color online) (a) Time series of the temperature at the point (0.0381, 0.097, 0.983) in the boundary layer near the hot wall at Ra = 12 600. [(b) and (c)] Streamlines on the plane $Y = 0$ at two arrow-pointed instants in (a): (b) $t = 8505$ and (c) $t = 8540$.

down to a periodic pulsation of three structures. The presence of hysteresis confirms that the spatial wave-number modulation instability is subcritical and supports the conjecture that the wave-number competition between mode 4 and mode 3 is similar to a subcritical Eckhaus instability.

Beyond Ra = 13 000, for $A_z = 10$, it is no longer possible to identify a discrete set of frequencies, and the flow rapidly becomes temporally chaotic. When Ra is increased to Ra = 15 000, the whole domain is still dominated by three structures, but patterns of two or four structures can also be observed, as evidenced by the evolution of the temperature spectral density $|\hat{T}(0,k)|^2$ for different wave numbers.

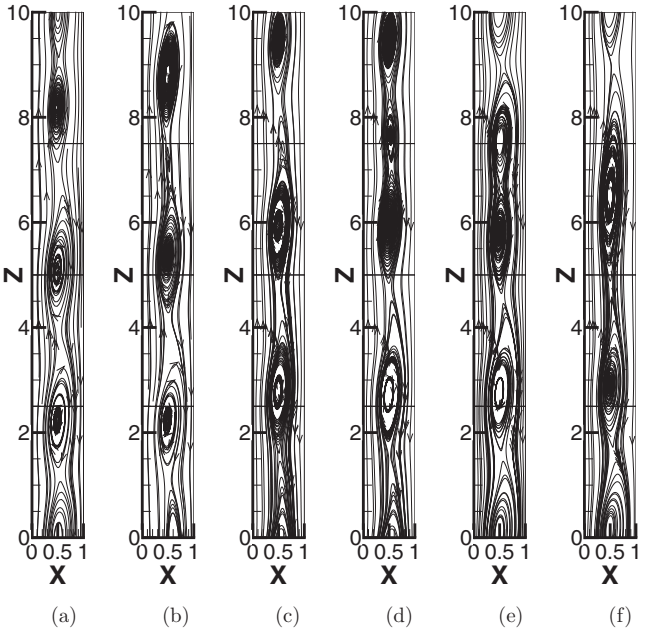

FIG. 20. Flow streamlines on the plane $y = 0$ at Ra = 12 200 for different times: (a) $t = 2905$; (b) $t = 2920$; (c) $t = 5900$; (d) $t = 5910$; (e) $t = 5960$; (f) $t = 5970$.

F. Influence of flow structures on global heat transfer

The global heat transfer is evaluated by the Nusselt number, which is defined as a ratio between the convective and diffusive heat transfer. In our simulations, the Nusselt number is calculated as $\mathrm{Nu} = \iint -\frac{\partial\langle\tilde{\theta}\rangle}{\partial x} dydz|_{x=0,1}$, since the velocity of the flow at the walls is zero, where $\langle\cdot\rangle$ denotes the time averaging of a variable. Its dependence with respect to the Rayleigh number Ra is plotted in Fig. 22.

In the 2D steady regime, we find that $\mathrm{Nu} \sim 0.0867\mathrm{Ra}^{0.25}$, which is consistent with the laminar regime. This estimate actually holds slightly beyond the second supercritical pitchfork bifurcation, where the 2D rolls become more intense and distorted in the transversal direction (this stage is labeled as "quasi-2D structures" in Fig. 22). However, at Ra = 10 500, the flow becomes three-dimensional through the creation of secondary vortices, and the Nusselt number experiences a small decrease. It then remains approximately constant over the 3D steady regime from Ra = 10 500 and Ra = 10 600. At the onset of the oscillatory regimes, the Nusselt number begins to increase and continues doing so over the sequence of period-doubling bifurcations. After a sharp decrease observed at the onset of the Eckhaus-like instability, the Nusselt number starts increasing again. The maximum heat transfer increases over the range of Rayleigh numbers Ra $<$ 15 000 is about 20%, which agrees with Wright *et al.*'s [21] results.

We note that the spatial characteristics of Wright *et al.*'s "secondary cells" match those of what we call primary rolls. Furthermore, their general description of the route to turbulence seems to agree loosely with ours, as their flow becomes three-dimensional and then chaotic at a Rayleigh number of 13 600, which is close to our observations. However, two discrepancies are observed: (i) unlike our stationary rolls, their cells appear to drift in the vertical direction from the onset of the first instability, which could be due to (horizontal) end effects of the cavity, and (ii) as the Rayleigh number increases, the motion of the cells is intensified, and merging between the cells occurred, whereas no vortex pairing was observed in our simulation. This difference could be the consequence of the relatively small dimensions of our numerical domain.

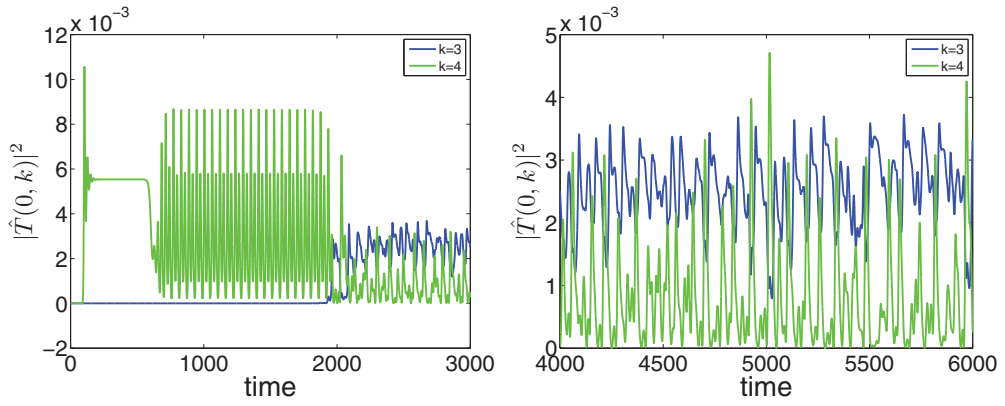

FIG. 21. (Color online) Temporal evolution of the spectral coefficients $|\hat{T}(0,k)|^2$ on the midplane $y = 0.5$ for selected modes k. [(a) and (b)] Ra $= 12\,300$, modes $k = 3,4$: (a) $t \in [0,3000]$ and (b) $t \in [4000,6000]$.

V. CONCLUSION

The focus of the present study is the sequence of instabilities leading to chaos for the air flow between two infinite differentially heated vertical plates. Our goal is to examine the influence of three-dimensional effects in transition. A mapping of the route to chaos has been established in two and in three dimensions. In both cases the base flow bifurcates to 2D steady rolls through a supercritical circle pitchfork bifurcation at $\mathrm{Ra}_c = 5708$. The nature of this first instability is found to be absolute. A weakly nonlinear analysis results in the derivation of a Ginzburg-Landau equation which is able to predict correctly the amplitude of the 2D rolls for Rayleigh numbers within a limited range (10%) of Ra_c.

In 2D simulations, a second bifurcation occurs at Ra = 13 500. The flow becomes oscillatory, and the steady four-roll pattern turns into a periodic three-roll one with a characteristic frequency $f = 0.032$. When Ra is increased, the temporal evolution of the three unsteady rolls becomes quasiperiodic, and then apparently chaotic, while the characteristic frequency f remains dominant. As Ra is further increased to Ra = 18 000, the flow becomes steady again, and the three oscillatory rolls give way to two steady rolls. This suggests that the occurrence of pure temporal chaos is limited by the development of a vertical instability, which leads to a long-wavelength modulation of the spatial pattern. The two steady rolls remain stable over a range of Rayleigh numbers, as no chaotic behavior is observed up to Ra = 21 000.

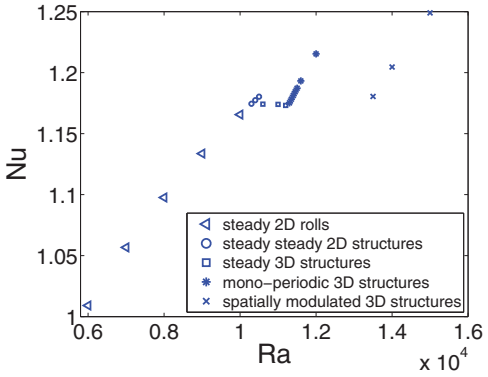

FIG. 22. (Color online) The Nusselt number Nu (averaged over vertical planes and time) as a function of Ra for $A_z = 10$.

The situation differs in 3D simulation (Table II). The second bifurcation is observed at a Rayleigh number of $\mathrm{Ra}_{c2} \sim 9980$. The 2D rolls become unstable through another supercritical pitchfork bifurcation to a steady 3D pattern, characterized by secondary counter-rotating vortices connecting the principal convection rolls. When the Rayleigh number is further increased to $\mathrm{Ra}_{c3} \sim 11\,270$, the steady 3D pattern becomes oscillatory through a Hopf bifurcation, as the intensities of the transverse rolls and the counter-rotating vortices oscillate in phase opposition. A sequence of period-doubling bifurcations is then observed at higher Rayleigh numbers. If the periodic height of the plates is small enough ($A_z = 2.5$), thereby preventing any modulation of the basic vertical wavelength, the period-doubling bifurcations lead to temporal chaos at Ra = 12 400. The location of the chaotically pulsating structures is observed to be intermittent beyond Ra > 12 550. For larger domains such as $A_z = 10$, the sequence of period-doubling bifurcations is also observed, but only as a transient feature. The multiply periodic flow gives way to complex spatiotemporal dynamics when Ra $\geqslant$ 12 100 and a competition between different wavelengths is rapidly apparent in the flow pattern. The global behavior of heat transfer is established up to Ra = 15 000, where Nu generally increases with Ra, with discontinuities as the flow goes through bifurcations.

Comparison of 2D and 3D results confirms that transverse effects are essential in the development of instabilities and the onset of chaos. This result is of interest, and as in many situations involving thermal convection, the first step towards making a problem tractable is to reduce it to a two-dimensional geometry. We emphasize that, due to numerical constraints, the dimensions of the plates were relatively small in the present study. The competition between vertical and transverse pattern modulations is expected to be altered as the dimensions of the plate increase. Comparison of the present study with experimental results highlights the need for larger simulation

TABLE II. Summary of bifurcations and associated flow structures and symmetries for 3D simulations, $A_z = 10$, $T = 1/f_1$.

Ra	Nature of bifurcation	Flow structures Number of structures	Spatial symmetry Temporal symmetry
$\mathrm{Ra} < \mathrm{Ra}_c = 5708$		1D base flow	$O(2) \times O(2)$ Steady
$\mathrm{Ra}_c < \mathrm{Ra} < 9980$	Supercritical Circle pitchfork	2D corotating rolls $n = 4$	$O(2) \times D_4$ Steady
$9980 < \mathrm{Ra} < 11\,270$	Supercritical Circle pitchfork	3D structures $n = 4$	$D_1 \times D_4$ Steady
$11\,270 < \mathrm{Ra} \leqslant 12\,000$	Supercritical Hopf	3D structures $n = 4$	$D_1 \times D_4$ T periodic
$\mathrm{Ra} \geqslant 12\,100$	Period doubling	3D structures $n = 4$	$D_1 \times D_4$ 2^nT periodic
	subcritical Eckhaus-like instability	3D structures $n = 3$	No Symmetry

domains, as well as for a better experimental characterization of transverse effects.

ACKNOWLEDGMENT

Some of the computations were carried out at CNRS-IDRIS Project DARI0326.

APPENDIX A: NUMERICAL METHODS

A multidomain spectral code [36] is used for our 3D simulation. The domain decomposition is based on the definition of a Schur complement and implemented with MPI library. Incompressibility of the flow is enforced by the projection-correction method. The spatial discretization is performed with the spectral collocation method, while the temporal discretization is carried out through a second-order implicit-explicit mixed scheme. The overall procedure consists of solving several general Helmholtz equations.

1. Discretization

The spectral collocation method is used for spatial discretization. In the horizontal direction x, Chebyshev modes are used. In the transverse direction y, Fourier modes are used, as the periodic boundary condition is imposed. The domain is divided into four subdomains along the vertical direction z. Chebyshev modes are used for each subdomain in this direction. A periodic communicator is defined through MPI to enforce the periodic vertical boundary condition over the full domain. The solution of Navier-Stokes equations in the interior of each subdomain is executed independently on a single processor. The continuity of variables and their first derivatives across the interface between the subdomains is ensured by defining a Schur complement method, where the Schur matrix is built using an influence matrix technique [36].

A second-order mixed explicit-implicit scheme is adopted for the temporal integration. The diffusive term is treated implicitly, while the convective term is calculated explicitly. The discretized Navier-Stokes equations can be recast into four general Helmholtz equations for u, v, w, θ, respectively,

$$\frac{\mathrm{Pr}}{\sqrt{\mathrm{Ra}}}\nabla^2 u^{n+1} - \frac{3}{2\Delta t}u^{n+1} = \frac{\partial p^{n+1}}{\partial x} - \frac{4u^n - u^{n-1}}{2\Delta t} + 2(\mathbf{V}\cdot\vec{\nabla}u)^n - (\mathbf{V}\cdot\vec{\nabla}u)^{n-1}, \tag{A1}$$

$$\frac{\mathrm{Pr}}{\sqrt{\mathrm{Ra}}}\nabla^2 v^{n+1} - \frac{3}{2\Delta t}v^{n+1} = \frac{\partial p^{n+1}}{\partial y} - \frac{4v^n - v^{n-1}}{2\Delta t} + 2(\mathbf{V}\cdot\vec{\nabla}v)^n - (\mathbf{V}\cdot\vec{\nabla}v)^{n-1}, \tag{A2}$$

$$\frac{\mathrm{Pr}}{\sqrt{\mathrm{Ra}}}\nabla^2 w^{n+1} - \frac{3}{2\Delta t}w^{n+1} = \frac{\partial p^{n+1}}{\partial z} - \frac{4w^n - w^{n-1}}{2\Delta t} + 2(\mathbf{V}\cdot\vec{\nabla}w)^n - (\mathbf{V}\cdot\vec{\nabla}w)^{n-1}, \tag{A3}$$

$$\frac{1}{\sqrt{\mathrm{Ra}}}\nabla^2\theta^{n+1} - \frac{3}{2\Delta t}\theta^{n+1} = -\frac{4\theta^n - \theta^{n-1}}{2\Delta t} + 2(\mathbf{V}\cdot\vec{\nabla}\theta)^n - (\mathbf{V}\cdot\vec{\nabla}\theta)^{n-1}. \tag{A4}$$

A fifth general Helmholtz equation for a potential needs to be solved in the procedure of the projection-correction method to ensure the incompressibility of the flow. All five general Helmholtz problems are solved by use of the matrix-diagonalization method, which is presented as follows.

2. Solution of the general Helmholtz problem

The general 3D Helmholtz problem reads as

$$(\nabla^2 - \lambda) f = S, \tag{A5}$$

where $\nabla^2 = \frac{\partial^2}{\partial x^2} + \frac{\partial^2}{\partial y^2} + \frac{\partial^2}{\partial z^2}$; $\lambda = \frac{3\sqrt{\mathrm{Ra}}}{2\mathrm{Pr}\Delta t}$ for u,v,w; $\lambda = \frac{3\sqrt{\mathrm{Ra}}}{2\Delta t}$ for θ; and S represents the source term. The idea solve this equation in the discrete form is to invert the operator

$(\nabla^2 - \lambda)$. In our code, the matrix-diagonalization method is employed [36,47,48]. In fact, the second derivative, for example $\frac{\partial^2}{\partial x^2}$, in the discrete form constitutes a regular matrix, which is diagonalizable and invertible, so we have $D_x^2 = P\Lambda_x P^{-1}$, $D_y^2 = Q\Lambda_y Q^{-1}$, $D_z^2 = R\Lambda_z R^{-1}$, where Λ_x, Λ_y, Λ_z are diagonal matrix containing the eigenvalues, and the matrices P, Q, R are formed by the eigenvectors of D_x^2, D_y^2, D_z^2, respectively. In the discrete forms, the 3D Helmholtz equation takes the following form:

$$\left(\mathbf{I}_z \otimes \mathbf{I}_y \otimes D_x^2 + \mathbf{I}_z \otimes D_y^2 \otimes \mathbf{I}_x + D_z^2 \otimes \mathbf{I}_y \otimes \mathbf{I}_x - \mathbf{I}_z \otimes \mathbf{I}_y \otimes \mathbf{I}_x\lambda\right)F = S, \tag{A6}$$

where $\otimes$ is the Kronecker product operator. Multiplying Eq. (A6) by $(P^{-1} \otimes Q^{-1} \otimes R^{-1})$, we can pass this equation into the eigenspace in the following way. For the first term on the left side of Eq. (A6), we have $(R^{-1} \otimes Q^{-1} \otimes P^{-1})(\mathbf{I}_z \otimes \mathbf{I}_y \otimes D_x^2) = (\mathbf{I}_z \otimes \mathbf{I}_y \otimes \Lambda_x)(R^{-1} \otimes Q^{-1} \otimes P^{-1})$ by using twice the property $(A \otimes B)(C \otimes D) = AC \otimes BD$. With similar treatment for the other terms, we can obtain

$$(\mathbf{I}_z \otimes \mathbf{I}_y \otimes \Lambda_x + \mathbf{I}_z \otimes \Lambda_y \otimes \mathbf{I}_x + \Lambda_z \otimes \mathbf{I}_y \otimes \mathbf{I}_x - \mathbf{I}_z \otimes \mathbf{I}_y \otimes \mathbf{I}_x\lambda)\tilde{F} = \tilde{S}, \tag{A7}$$

where $\tilde{F} = (R^{-1} \otimes Q^{-1} \otimes P^{-1})F$ and $\tilde{S} = (R^{-1} \otimes Q^{-1} \otimes P^{-1})S$. Therefore, to solve the 3D Helmholtz problem, we first multiply the source term S by $(R^{-1} \otimes Q^{-1} \otimes P^{-1})$ to obtain $\tilde{S}$. Then $\tilde{F}$ can be easily obtained by inverting the operator in front of $\tilde{F}$ in Eq. (A7). Finally, multiplying $\tilde{F}$ by $P \otimes Q \otimes R$, we get the solution F.

APPENDIX B: OPERATORS IN MULTISCALE ANALYSIS SECTION

The operators defined in Eqs. (15) to (17) can be expressed as

$$M_0 = \begin{bmatrix} \nabla_0^2 & 0 \\ 0 & 1 \end{bmatrix}, \tag{B1}$$

$$M_1 = \begin{bmatrix} 2\frac{\partial}{\partial z_0}\frac{\partial}{\partial z_1} & 0 \\ 0 & 0 \end{bmatrix}, \tag{B2}$$

$$M_2 = \begin{bmatrix} \frac{\partial^2}{\partial z_1^2} & 0 \\ 0 & 0 \end{bmatrix}, \tag{B3}$$

$$L_0 = \begin{bmatrix} \frac{\mathrm{Pr}}{\sqrt{\mathrm{Ra}_c}}\nabla_0^4 - W\frac{\partial}{\partial z_0}\nabla_0^2 + \frac{\partial^2 W}{\partial x^2}\frac{\partial}{\partial z_0} & \mathrm{Pr}\frac{\partial}{\partial x} \\ \frac{\partial \Theta}{\partial x}\frac{\partial}{\partial z_0} & \frac{1}{\sqrt{\mathrm{Ra}_c}}\nabla_0^2 - W\frac{\partial}{\partial z_0} \end{bmatrix}, \tag{B4}$$

$$L_1 = \begin{bmatrix} 4\frac{\mathrm{Pr}}{\sqrt{\mathrm{Ra}_c}}\frac{\partial}{\partial z_0}\frac{\partial}{\partial z_1}\nabla_0^2 - W\frac{\partial}{\partial z_1}\nabla_0^2 - 2W\frac{\partial}{\partial z_1}\frac{\partial^2}{\partial z_0^2} + \frac{\partial^2 W}{\partial x^2}\frac{\partial}{\partial z_1} & 0 \\ \frac{\partial \Theta}{\partial x}\frac{\partial}{\partial z_1} & \frac{2}{\sqrt{\mathrm{Ra}_c}}\frac{\partial}{\partial z_0}\frac{\partial}{\partial z_1} - W\frac{\partial}{\partial z_1} \end{bmatrix}, \tag{B5}$$

$$L_2 = \begin{bmatrix} 2\frac{\mathrm{Pr}}{\sqrt{\mathrm{Ra}_c}}\frac{\partial^2}{\partial z_1^2}\left(\nabla_0^2 + 2\frac{\partial^2}{\partial z_0^2}\right) - 3W\frac{\partial}{\partial z_0}\frac{\partial^2}{\partial z_1^2} & 0 \\ 0 & \frac{1}{\sqrt{\mathrm{Ra}_c}}\frac{\partial^2}{\partial z_1^2} \end{bmatrix} + \begin{bmatrix} -\frac{1}{2}\frac{\mathrm{Pr}}{\sqrt{\mathrm{Ra}_c^3}}\nabla_0^4 - \frac{W}{2\mathrm{Ra}_c}\frac{\partial}{\partial z_0}\nabla_0^2 + \frac{1}{2\mathrm{Ra}_c}\frac{\partial^2 W}{\partial x^2}\frac{\partial}{\partial z_0} & 0 \\ 0 & -\frac{1}{2}\frac{1}{\sqrt{\mathrm{Ra}_c^3}}\nabla_0^2 - \frac{W}{2\mathrm{Ra}_c}\frac{\partial}{\partial z_0} \end{bmatrix}, \tag{B6}$$

$$b_{0,\psi}(\phi_\alpha, \phi_\beta) = \left(\frac{\partial \psi_\alpha}{\partial z_0}\frac{\partial}{\partial x} - \frac{\partial \psi_\alpha}{\partial x}\frac{\partial}{\partial z_0}\right)\nabla_0^2 \psi_\beta, \tag{B7}$$

$$b_{0,\theta}(\phi_\alpha, \phi_\beta) = \left(\frac{\partial \psi_\alpha}{\partial z_0}\frac{\partial}{\partial x} - \frac{\partial \psi_\alpha}{\partial x}\frac{\partial}{\partial z_0}\right)\theta_\beta, \tag{B8}$$

$$b_{1,\psi}(\phi_\alpha, \phi_\beta) = \left(\frac{\partial \psi_\alpha}{\partial z_1}\frac{\partial}{\partial x} - \frac{\partial \psi_\alpha}{\partial x}\frac{\partial}{\partial z_1}\right)\nabla_0^2 \psi_\beta + 2\left(\frac{\partial \psi_\alpha}{\partial z_0}\frac{\partial}{\partial x} - \frac{\partial \psi_\alpha}{\partial x}\frac{\partial}{\partial z_0}\right)\frac{\partial}{\partial z_0}\frac{\partial}{\partial z_1}\psi_\beta, \tag{B9}$$

$$b_{1,\theta}(\phi_\alpha, \phi_\beta) = \left(\frac{\partial \psi_\alpha}{\partial z_1}\frac{\partial}{\partial x} - \frac{\partial \psi_\alpha}{\partial x}\frac{\partial}{\partial z_1}\right)\theta_\beta, \tag{B10}$$

where $\nabla_0 = \frac{\partial^2}{\partial x^2} + \frac{\partial^2}{\partial z_0^2}$, Ra_c is the critical Rayleigh number found in the linear stability analysis, W is the vertical velocity of the base flow, and Θ is the temperature of the base flow.

[1] P. Manneville, Dyn. Spatio-Temp. Cellular Struct. **207**, 41 (2006).
[2] J. Elder, J. Fluid Mech. **23**, 77 (1965).
[3] C. Vest and V. Arpaci, J. Fluid Mech. **36**, 1 (1969).
[4] Y. Oshima, J. Phys. Soc. Jpn. **30**, 872 (1971).
[5] G. K. Batchelor, Quart. Appl. Math. **12**, 209 (1954).
[6] A. Gill and A. Davey, J. Fluid Mech. **35**, 775 (1969).
[7] R. Bergholz, J. Fluid Mech. **84**, 743 (1978).
[8] P. Daniels and M. Weinstein, J. Eng. Math. **24**, 179 (1989).
[9] J. Cornet and C. Lamarque, Mech. Res. Comm. **24**, 179 (1997).
[10] J. Mizushima and K. Gotoh, J. Phys. Soc. Jpn. **52**, 1206 (1983).
[11] J. Mizushima and Y. Saito, Fluid Dyn. Res. **2**, 183 (1987).
[12] J. Mizushima and H. Tanaka, Phys. Fluids **14**, L21 (2002).
[13] J. Mizushima and H. Tanaka, J. Phys. Soc. Jpn. **71**, 2898 (2002).
[14] S. Xin, Ph.D. thesis, Université Paris VI, 1993.
[15] D. R. Chenoweth and S. Paolucci, Phys. Fluids **28**, 2375 (1985).
[16] D. R. Chenoweth and S. Paolucci, J. Fluid Mech. **169**, 173 (1986).
[17] P. L. Quéré, ASME J. Heat Transf. **112**, 965 (1990).
[18] S. Wakitani, Phys. Fluids. **10**, 1924 (1998).
[19] H. Gunes, Fluid Dyn. Res. **30**, 1 (2002).
[20] B. Lartigue, S. Lorente, and B. Bourret, Int. J. Heat Mass Transf. **43**, 3157 (2000).
[21] J. L. Wright, H. Jin, K. G. T. Hollands, and D. Naylor, Int. J. Heat Mass Transf. **49**, 889 (2006).
[22] A. Chait and S. Korpela, J. Fluid Mech. **200**, 189 (1989).
[23] M. Nagata and F. Busse, J. Fluid Mech. **135**, 1 (1983).
[24] R. M. Clever and F. H. Busse, Chaos Soliton. Fract. **5**, 1795 (1995).
[25] A. Suslov and S. Paolucci, Fluid Dyn. Res. **35**, 159 (2004).
[26] A. Suslov and S. Paolucci, J. Fluid Mech. **344**, 1 (1997).
[27] D. A. Bratsun, A. V. Zyuzgin, and G. F. Putin, Int. J. Heat Fluid Flow **24**, 835 (2003).
[28] J. R. Phillips, Int. J. Heat Mass Transf. **39**, 2485 (1996).
[29] J. Elder, J. Fluid Mech. **23**, 99 (1965).
[30] T. Versteegh and F. Nieuwstadt, Int. J. Heat Fluid Flow **19**, 135 (1998).
[31] T. Versteegh and F. Nieuwstadt, Int. J. Heat Mass Transf. **42**, 3673 (1999).
[32] M. Wang, S. Fu, and G. Zhang, Phys. Rev. E **66**, 066306 (2002).
[33] P. Hall, J. Fluid Mech. **703**, 99 (2012).
[34] A. Sergent and P. L. Quéré, J. Phys. Conf. Ser. **318**, 082010 (2011).
[35] B. Podvin and A. Sergent, Phys. Fluids **23**, 105106 (2012).
[36] S. Xin, J. Chergui, and P. L. Quéré, in *Parallel Computational Fluid Dynamics 2008*, edited by D. Tromeur-Dervout, G. Brenner, D. Emerson, and J. Erhel, Lecture Notes in Computational Science and Engineering Vol. 74 (Springer, Berlin, 2008), pp. 163–172.
[37] D. W. Ruth, Int. J. Heat Mass Transf. **22**, 1199 (1979).
[38] C. Cossu, Lecture Notes, Ecole Polytechnique, Palaiseau, France (2009).
[39] J. Tao and F. Zhuang, Phys. Rev. E **62**, 7957 (2000).
[40] R. Henderson and D. Barkley, Phys. Fluids **8**, 1683 (1996).
[41] J. C. R. Hunt, A. A. Wray, and P. Moin, in *Studying Turbulence Using Numerical Simulation Databases, 2*, Vol. 1 (Center for Turbulence Research, Stanford University, 1988), pp. 193–208.
[42] C. Ho and P. Huerre, Ann. Rev. Fluid Mech. **16**, 365 (1984).
[43] J. Maurer and A. Libchaber, Le J. Phys. Lett. **40**, 419 (1979).
[44] M. Giglio, S. Musazzi, and U. Perini, Phys. Rev. Lett. **47**, 243 (1981).
[45] D. Armbruster, J. Guckenheimer, and P. Holmes, Physica D **29**, 257 (1987).
[46] I. Melbourne, P. Chossat, and M. Golubitsky, Proc. R. Soc. Edin. A Math. **113**, 315 (1989).
[47] G. Labrosse, *Méthodes spectrales: méthodes locales, méthodes globales, problèmes d'Helmoltz et de Stokes, équations de Navier-Stokes* (Ellipses, 2011), Chap. 12, pp. 168–170.
[48] P. Haldenwang, G. Labrosse, S. Abboudi, and M. Deville, J. Comput. Phys. **55**, 115 (1984).